

We are IntechOpen, the world's leading publisher of Open Access books Built by scientists, for scientists

6,300

Open access books available

171,000

International authors and editors

190M

Downloads

Our authors are among the

154

Countries delivered to

TOP 1%

most cited scientists

12.2%

Contributors from top 500 universities



WEB OF SCIENCE™

Selection of our books indexed in the Book Citation Index
in Web of Science™ Core Collection (BKCI)

Interested in publishing with us?
Contact book.department@intechopen.com

Numbers displayed above are based on latest data collected.
For more information visit www.intechopen.com



Evaluation of the Long-Term Stability of Metrology Instruments

Romain Coulon

Abstract

This chapter aims to emphasize the issue of the long-term stability of instruments used in metrology. This issue is a concern mentioned in the IEC/ISO17025:2017 standard and the JCGM100:2008 guide. Control charts are mentioned in these key documents as tools to assess whether a measurement process is under statistical control or not. Control charts (Shewhart charts, CUSUM chart, EWMA chart) are introduced and tested with simulated and real datasets from metrology instruments that operate at the ionizing department of the BIPM. The interest and the limits of such statistical analysis are discussed. They take their basis in a measurement model composed of Gaussian white noise. Although a measurement monitored over a relatively short period may be consistent with this model, it has been observed that the autocorrelation of the measurement data acquired over a long period limits the relevance of control charts. In this case, time series analysis seems more appropriate than conventional control charts. As an illustration, an optimal Bayesian smoother is introduced to demonstrate how to deconvolve the low-frequency random noise and refine the evaluation of uncertainty according to the measurement model for long-term measurement.

Keywords: metrology, control charts, time series, statistical control, long-term stability

1. Introduction

Long-term reproducibility in experimental sciences is a critical metrological topic recently discussed in [1]. In laboratories, the quality system is the frame in which such an issue is controlled. It is notably required in the ISO/IEC 17025 [2] that laboratories must ensure the validity of their results. For this, monitoring of the state of operating of a measurement system must be set up by periodic checks and statistical analysis of the obtained process control value.

Techniques to assess the reproducibility of a process is a matter of concern since the industrial era. An important step has been taken in 1924 with the invention of control charts by Walter Andrew Shewhart (Bell Telephone). Control charts are efficient tools to control if a process is under statistical control and is now widely used in many domains and recognized by the Project Management Institute as one of the seven basic tools of quality [3]. Moreover, control charts are explicitly proposed in ISO/IEC 17025 [2] and the JCGM100:2008 Guide [4] as tools to implement to analyze periodic checks using control standards.

The main advantages of control charts are their simplicity of implementation and their generic use, independent of the domains. A control chart displays a set of points and control limits. This representation makes it easy to check the number of points exceeding the control limits. Therefore, control charts can be analyzed by anybody without any specific skills in statistics.

Four typical control charts are introduced in this document: the original Shewhart charts (x-chart and R-chart), the CUSUM chart, and the EWMA chart. The manners that they are introduced below should be considered as examples that can slightly vary from one reference to another [5, 6]. These techniques are applied below to simulated data and real data from metrology instruments used in ionizing radiation metrology. Then, the interest of time series analysis is highlighted for the monitoring of measures over a long period using the same datasets.

2. Introduction to control charts

2.1 The x-chart

Periodical control using a check standard consists of periodically reproduce the measurement x_i at the time t_i and forms the measurement set $(x_1, x_2, \dots, x_i, \dots, x_N)$ where x_N is the last recorded point. In the x-chart, a central line is drawn by the moving empirical average \bar{x}_N over a period of 31 samples such as

$$\begin{cases} \bar{x}_N = \frac{\sum_{i=1}^N x_i}{N}, & \text{for } N \leq 31 \\ \bar{x}_N = \frac{\sum_{i=N-31}^N x_i}{31}, & \text{for } N > 31. \end{cases} \quad (1)$$

The control limits (LCL and UCL) are given by the multiple of the standard deviations:

$$\begin{cases} s(x_N) = \sqrt{\frac{\sum_{i=1}^N (x_i - \bar{x}_N)^2}{N - 1}}, & \text{for } N \leq 31, \\ s(x_N) = \sqrt{\frac{\sum_{i=N-31}^N (x_i - \bar{x}_N)^2}{30}}, & \text{for } N > 31, \end{cases} \quad (2)$$

such as

$$\begin{cases} \text{LCL} = \bar{x}_N - ks(x_N) \\ \text{UCL} = \bar{x}_N + ks(x_N), \end{cases} \quad (3)$$

where the multiplication factor k is set equal to 2 for the first control level and 3 for the second control level.

Failure criteria are defined according to a white Gaussian model that will be introduced later. It is important to note that the relevance of the analysis is low when the number of measures $N < 10$, relevant for $10 \leq N \leq 31$, and good for $N \geq 31$. Some criteria can be founded in the ISO 7870 standard [5]. As an example, the following rules are proposed where a measurement process is not considered under statistical control when:

- more than 0.35% of the points are above or below the control limits with the multiplication factor $k = 3$,
- more than 20% of the points are above or below the control limits with the multiplication factor $k = 2$,
- more than 9 points are in a row one side of \bar{x}_N ,
- more than 6 points are in a row increasing or decreasing,
- more than 14 points are in a row alternating between increase and decrease.

2.2 The R-chart

In the R-chart, the plotted points R_i are the derivatives of the measurements:

$$R_i = x_i - x_{i-1} \text{ for all } i \in \llbracket 2, N \rrbracket. \quad (4)$$

The central line and two levels of control limits are obtained in the same manner as for the x-chart by calculating the moving empirical average and standards deviations of the values R_i . Also, the same failure criteria can be applied.

2.3 The CUSUM chart

The cumulative of deviations C_i is obtained by the following recursive formula:

$$C_i = C_{i-1} + x_i - \bar{x}_N \quad (5)$$

In this chart, no central line is displayed but two control limits V_i are defined by the so-called V-mask:

$$V_i = C_N \pm ks(x_i)(d + N - i) \quad (6)$$

where $k = 0.1$ and $d = 147.22$.

Any points out of the V-mask mean that a significant drift of the process control value is detected.

2.4 The EWMA chart

The EWMA chart is obtained by plotting the exponentially smoothed data points z_i by using the following recursive formula:

$$z_i = \lambda x_i + (1 - \lambda) z_{i-1} \quad (7)$$

And where λ is a smoothing parameter.

The control limits CL are defined by

$$CL_i = \bar{x}_i \pm 3s(x_i) \sqrt{\frac{\lambda}{2 - \lambda} \left(1 - (1 - \lambda)^{2i} \right)} \quad (8)$$

With the smoothing parameter $\lambda = 2/N$.

Any point out of these control limits means that a significant drift of the process control value is detected.

It must be noted that these two families of control charts, the Shewhart charts on the one hand and the CUSUM and EWMA charts on the other hand, are complementary.

Indeed, the Shewhart charts aim to detect only large shifts above $1.5 s(x_i)$ (detection of outliers), whereas the CUSUM and EWMA charts aim to detect only small shifts below $1.5 s(x_i)$ and more generally drifts in the process. In other words, Shewhart charts perform an analysis in the high-frequency domain, whereas the CUSUM and EWMA charts are more suitable to analyze in the low-frequency domain.

3. Test of control charts with simulated data

3.1 The Gaussian white noise model

$N = 100$ normally distributed data points x_i are simulated using the random generator from the numpy.py library.

The model of the simulated process is the following:

$$\begin{cases} x_i = \mu_i + \varepsilon_i \\ \varepsilon_i \sim \mathcal{N}(0, \sigma_i^2) \end{cases} \tag{9}$$

with μ_i : the expectation parameter at the time t_i , \mathcal{N} : the normal distribution, and σ_i^2 : the variance parameter of the measurement noise ε_i at the time t_i . It is referred below as a Gaussian white noise model.

The reference dataset is defined by setting, for all $i \in \llbracket 1, N \rrbracket$, the parameters $\mu_i = 0$ and $\sigma_i^2 = 1$. The control charts are presented below, and the tests conclude—as expected—that the simulated process is under statistical control (Figures 1–4).

3.2 The Gaussian white noise model with a deterministic drift

Now, a slight positive drift is considered in the following model referred to as a deterministic drift model in a Gaussian white noise such as the expectation parameter takes values such as:

$$\begin{cases} \mu_i = 0, & \forall i \in \llbracket 1, \frac{N}{2} \rrbracket \\ \mu_i = \mu_{i-1} + 0.3, & \forall i \in \llbracket \frac{N}{2} + 1, N \rrbracket. \end{cases} \tag{10}$$

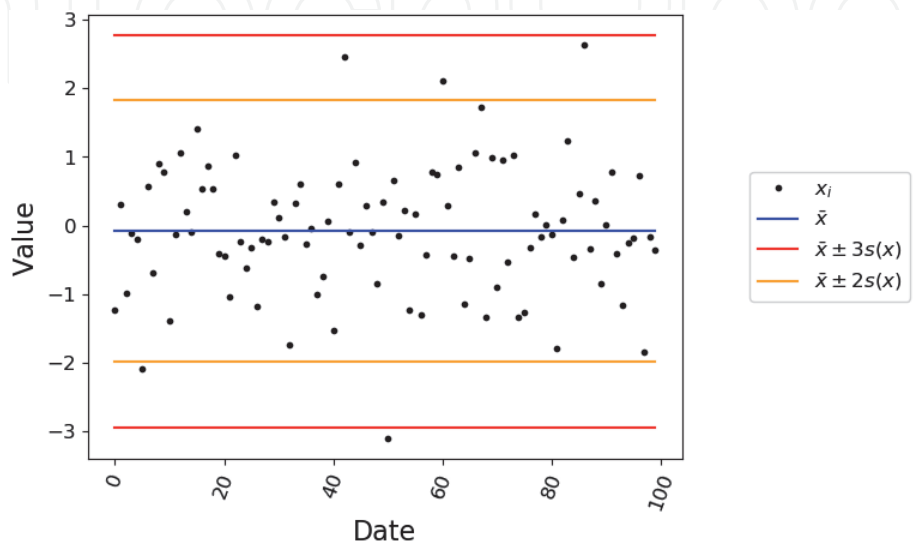


Figure 1. x-chart of the process simulated from the Gaussian white noise model.

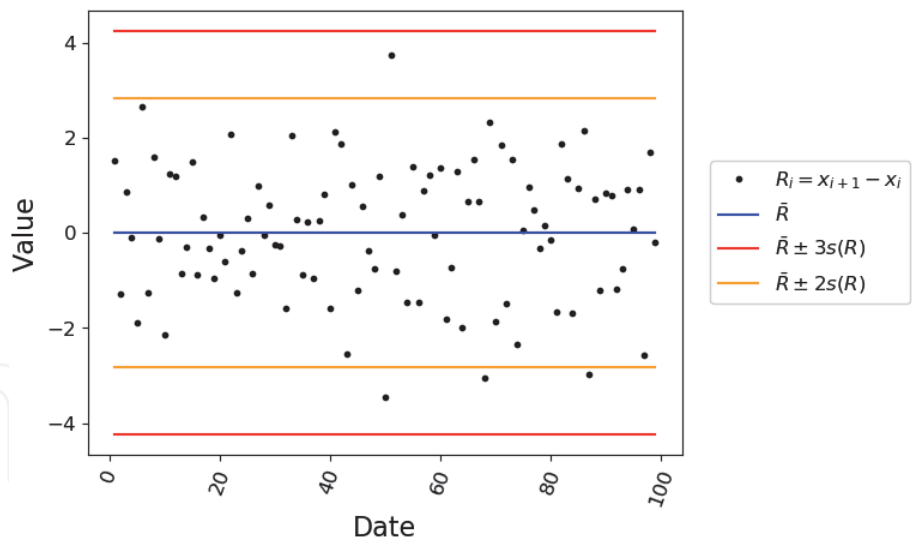


Figure 2.
R-chart of the process simulated from the Gaussian white noise model.

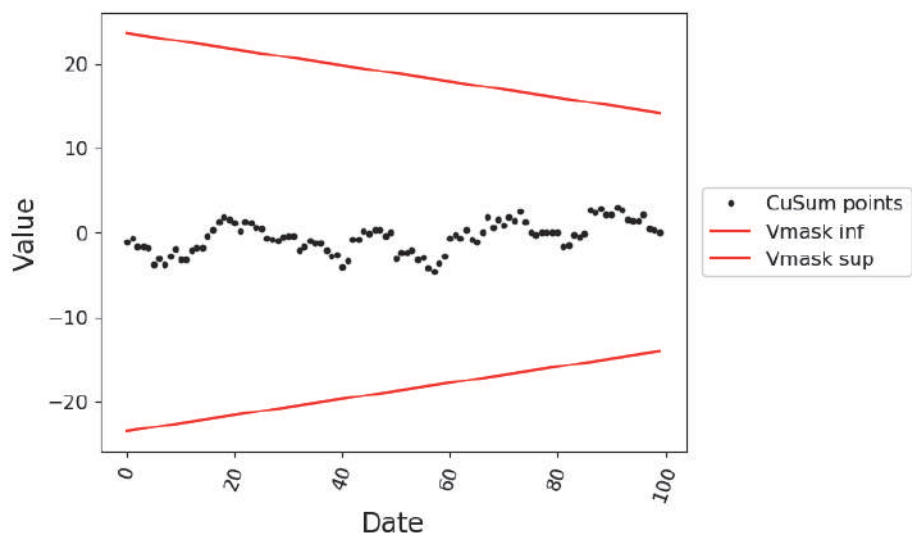


Figure 3.
CUSUM chart of the process simulated from the Gaussian white noise model.

This leads to a detection of this trend in the x-chart because more than nine points are in a row on one side of the central line. Also, the CUSUM chart and the EWMA chart detect the trend with some points out of their control limits (Figures 5–8).

3.3 The autocorrelated model

The third model studied here is the autocorrelated model (or the colored noise model) where a low-frequency Brownian noise is introduced in the following autocorrelated model:

$$\begin{cases} x_i = x_{i-1} + \dot{x}_i + \varepsilon_i \\ \dot{x}_i = \dot{x}_{i-1} + \delta_i \end{cases} \quad (11)$$

where the measurement noise is $\varepsilon_i \sim \mathcal{N}(0, \sigma_i^2)$ (idem as in Eq. (9)) and a process noise $\delta_i \sim \mathcal{N}(0, \tau_i^2)$ is added with a variance parameter τ_i^2 . In the example below, $\tau_i = 0.3$ while σ_i is still equal to 1.

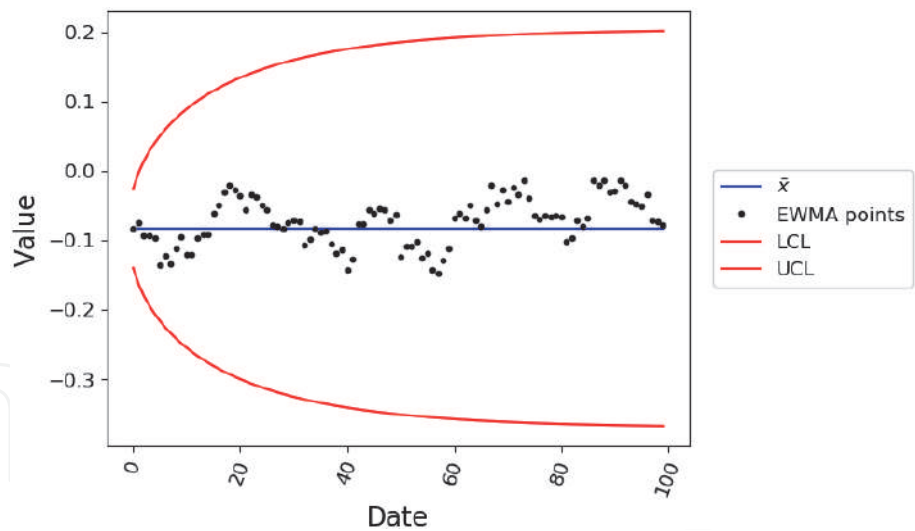


Figure 4.
EWMA chart of the process simulated from the Gaussian white noise model.

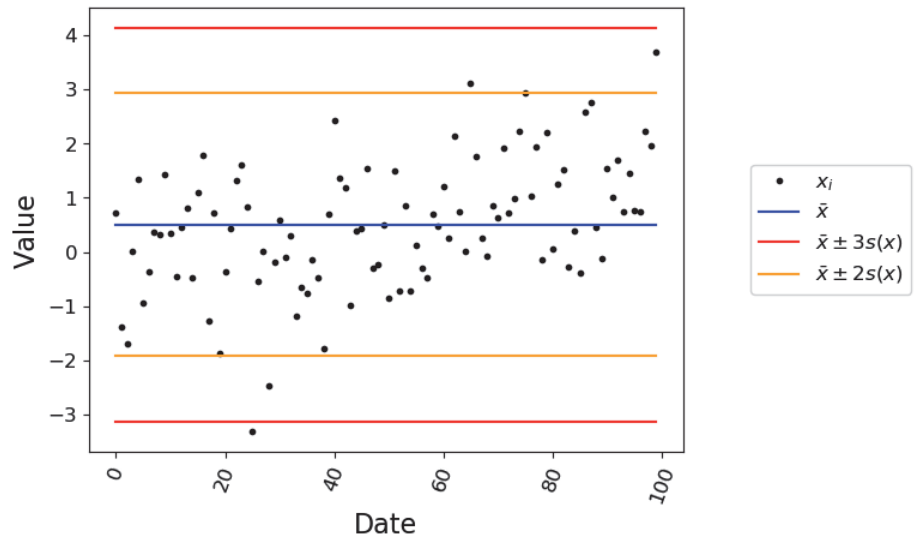


Figure 5.
 \bar{x} -chart of the process simulated from the Gaussian white noise model with a slight drift.

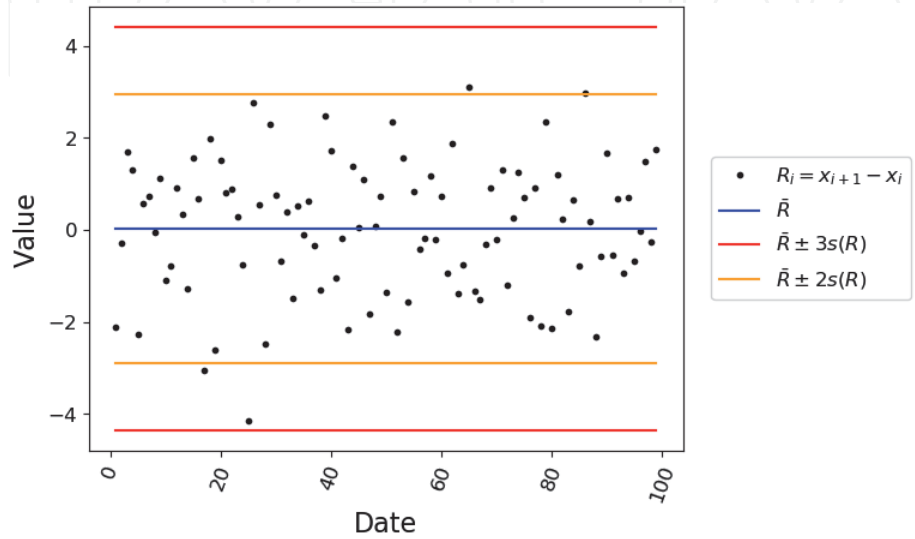


Figure 6.
R-chart of the process simulated from the Gaussian white noise model with a slight drift.

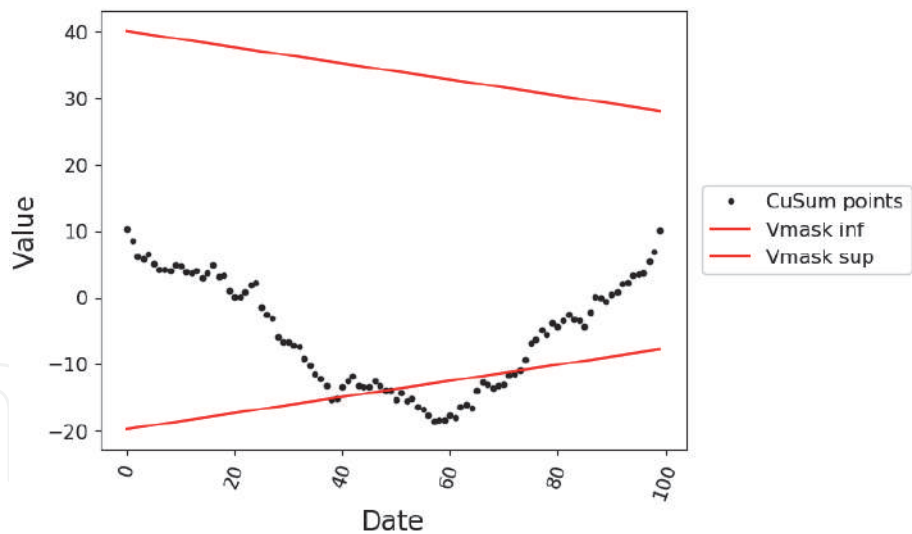


Figure 7.
CUSUM chart of the process simulated form the Gaussian white noise model with a slight drift.

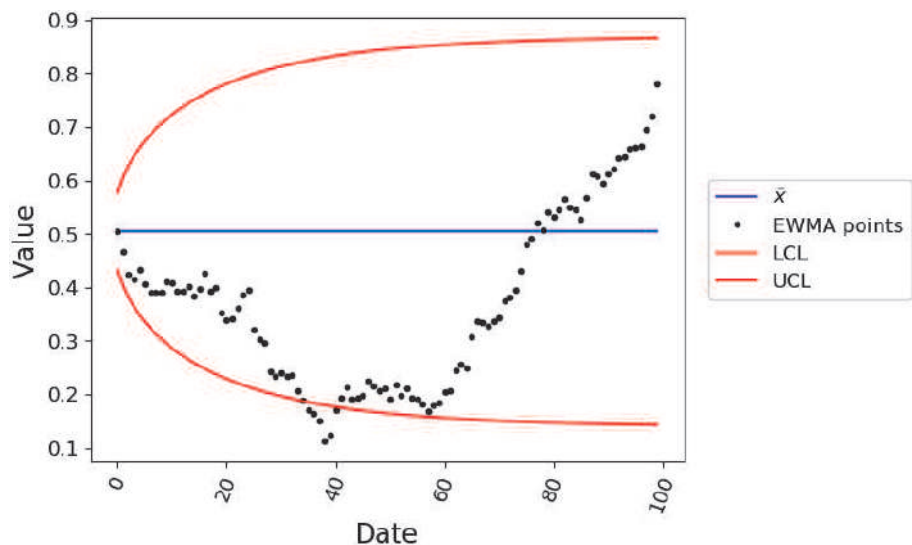


Figure 8.
EWMA chart of the process simulated form the Gaussian white noise model with a slight drift.

Again, this type of deviation from the Gaussian white noise model is detected by the value chart with more than nine points in a row on one side of the central line and by CUSUM and EWMA charts (**Figures 9–12**).

These three examples underline the fact that control charts are—by definition—build to verify whether a dataset fits with a Gaussian white noise model or not. Any deviation from this model is efficiently revealed by control charts. An operator could therefore conclude by the fact that the process is not under statistical control. This conclusion is good in the case of deterministic trends that are that a metrology system seeks to avoid maintaining the references that it produces. However, it has been demonstrated that the autocorrelated noise could also lead to an alert by control charts. On the contrary to the deterministic drift, the latter is a natural random process that appears in every system, which is observed on enough long-term periods. This particular limit of control charts was already pointed out by many authors [7–10]. This issue is an emphasis in the real cases presented below.

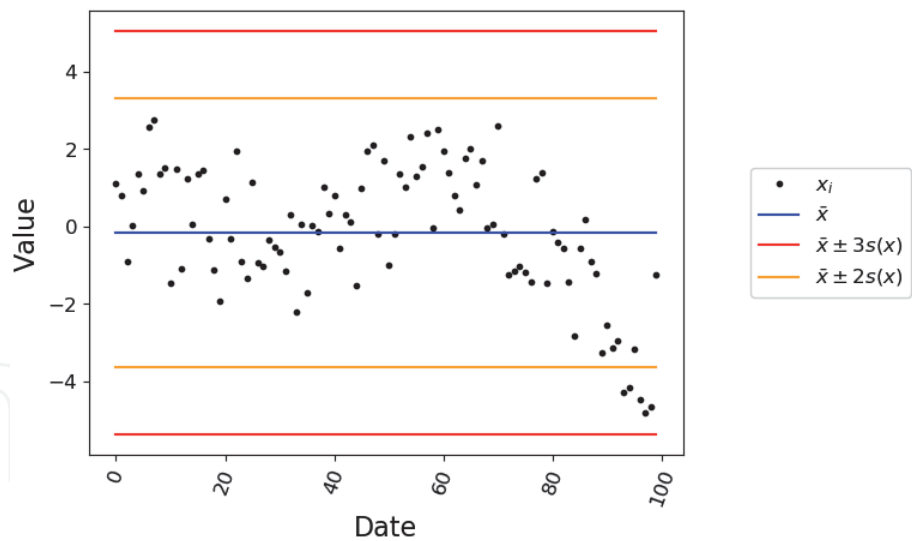


Figure 9.
 \bar{x} -chart of the process simulated form the autocorrelated model.

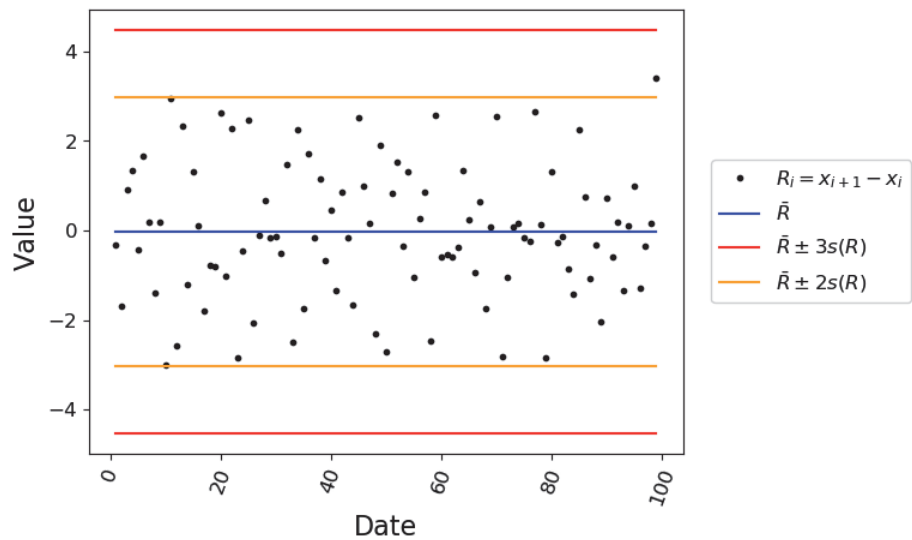


Figure 10.
Range chart of the process simulated form the autocorrelated model.

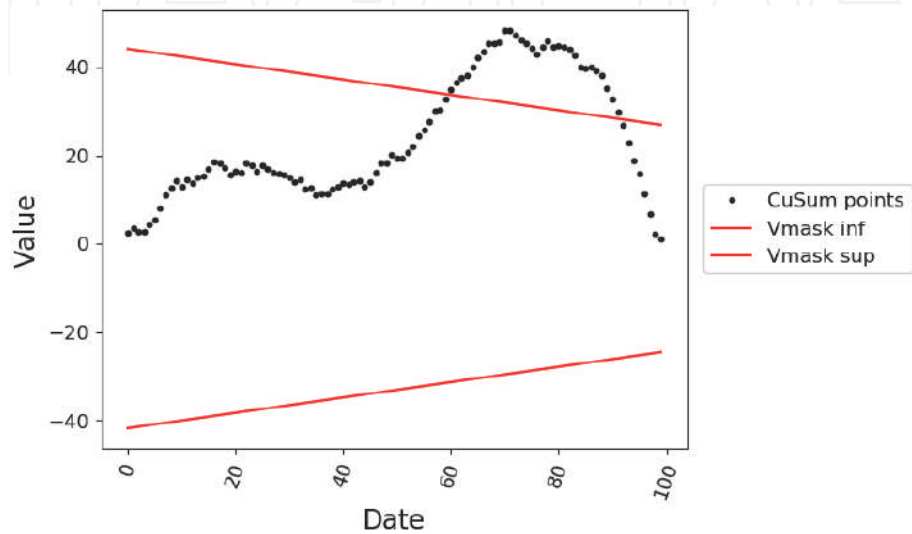


Figure 11.
CUSUM chart of the process simulated form the autocorrelated model.

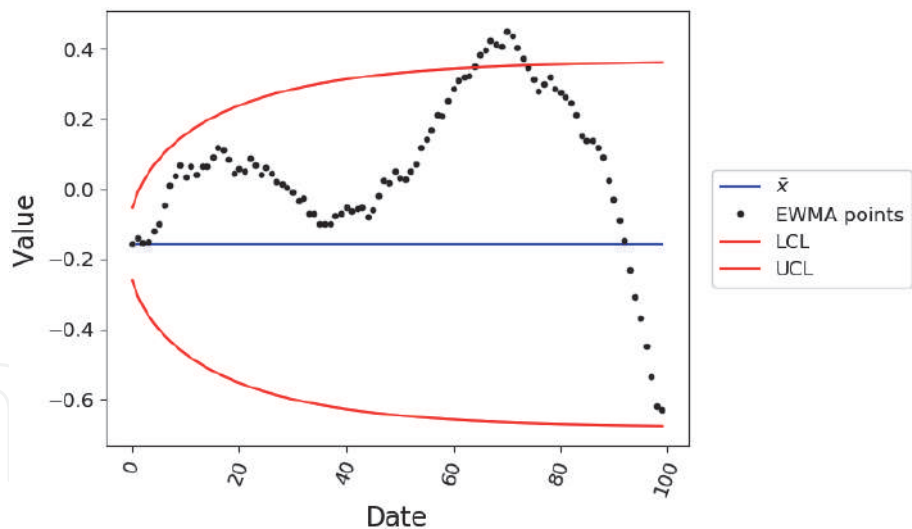


Figure 12.
EWMA chart of the process simulated from the autocorrelated model.

4. Test of control charts with real data

Two data are here considered. The first one comes from the periodic control of a recent metrology system that operates at the BIPM for radionuclide metrology and is called the ESIR (extended SIR) [11, 12]. The second example comes from the periodic control of a metrology service, the SIR, which operates at the BIPM for radionuclide metrology since 1976 [13].

4.1 Test with 1-year period data

The ESIR is under development, and the periodical control using check standards has been set up for 1 year. **Figures 13–16** show the analysis of the measured data by control charts. The monitored value is a comparison indicator obtained by using a check source of ^{14}C . The analysis from the four-control charts leads to the conclusion that the process is under statistical control. In other words, the measurement model complies with a Gaussian white noise model. At least, it is true for this short period of observation. The activity estimation is of the ^{14}C check source is stable and equal to 24.3373 ± 0.0184 A.U. There is no unit associated with the

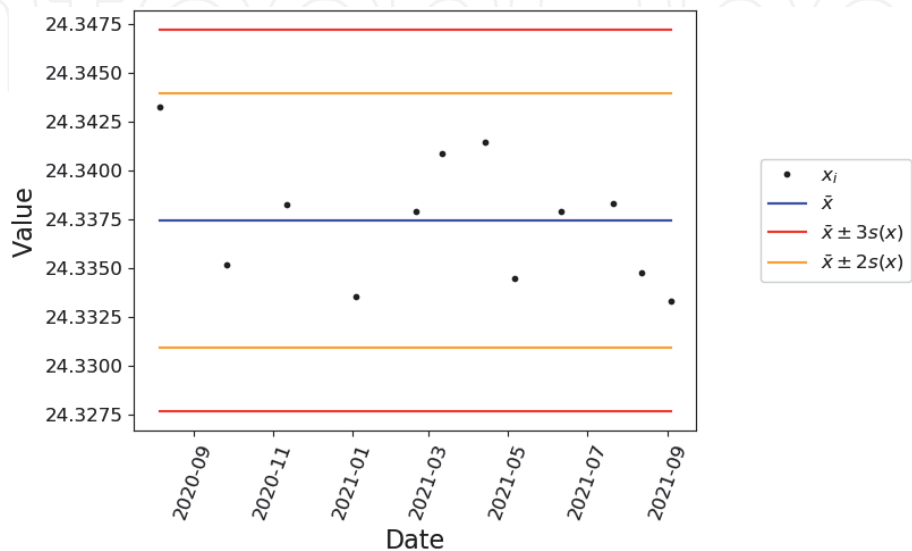


Figure 13.
 \bar{x} -chart of the periodic control of the ESIR metrology system.

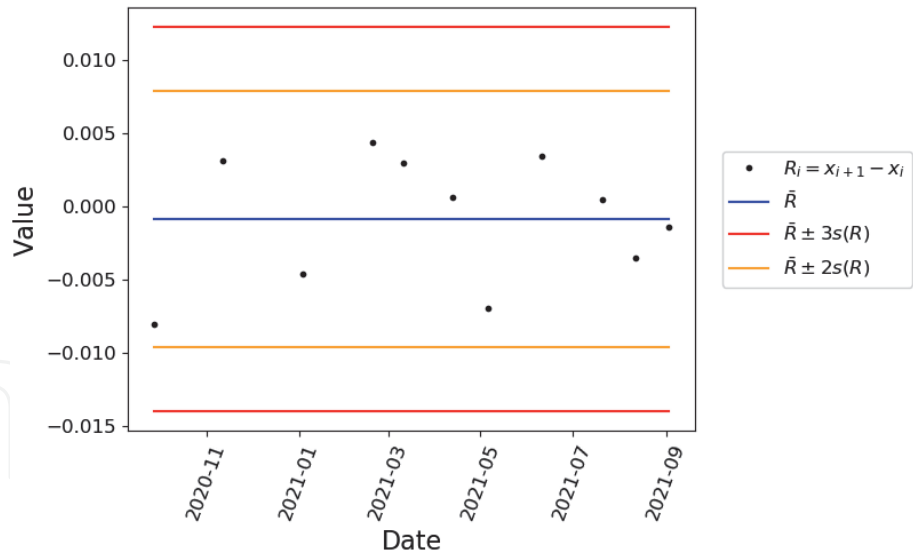


Figure 14.
R-chart of the periodic control of the ESIR metrology system.

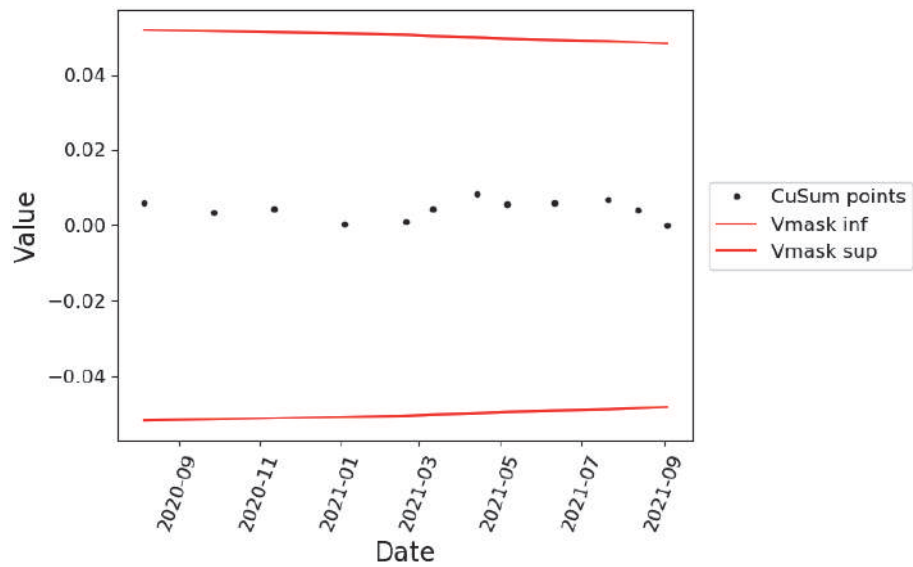


Figure 15.
CUSUM chart of the periodic control of the ESIR metrology system.

measurand because the aim of the ESIR is only to deliver a measure proportional to the activity but is very reproducible during the time. The relative standard uncertainty associated with this measurement is about 0.08%.

4.2 Test with 20-year period data

The SIR produces international references for decades. The ^{226}Ra source is used as a control standard to monitor the reproducibility of the measured current. In this case, the control charts are applied to a 20-year period of data acquisition. They have detected that the process is not under statistical control. However, these low-frequency fluctuations could certainly be a random colored noise and not a deterministic drift. This phenomenon appears when measurement values are observed over a very long period such as here. The only conclusion that can be drawn from control charts is that the data do not fit with the Gaussian white noise model and that a type A evaluation of the uncertainty associated with the measurement values (from t_1 to t_N) cannot be applied. Nevertheless, it is no need to refine

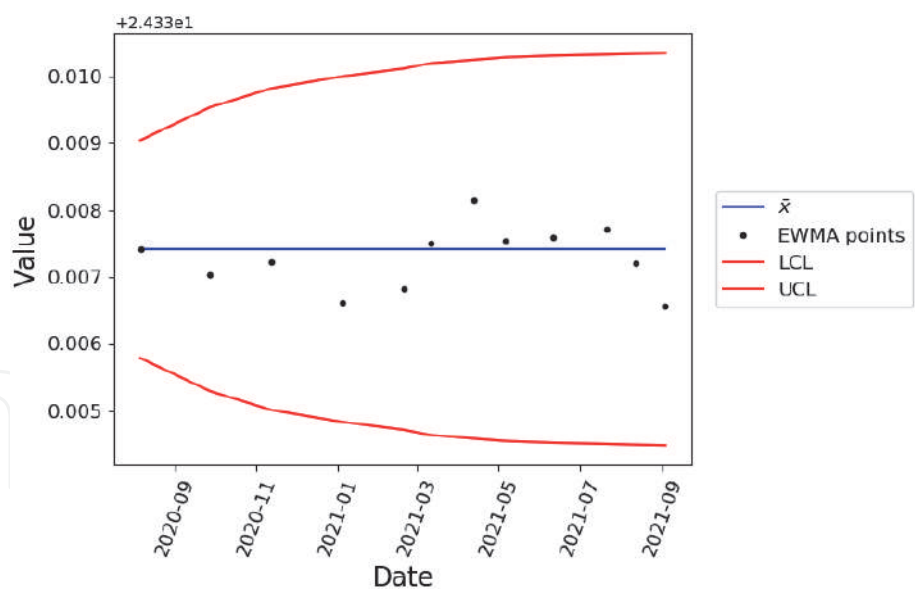


Figure 16.
EWMA chart of the periodic control of the ESIR metrology system.

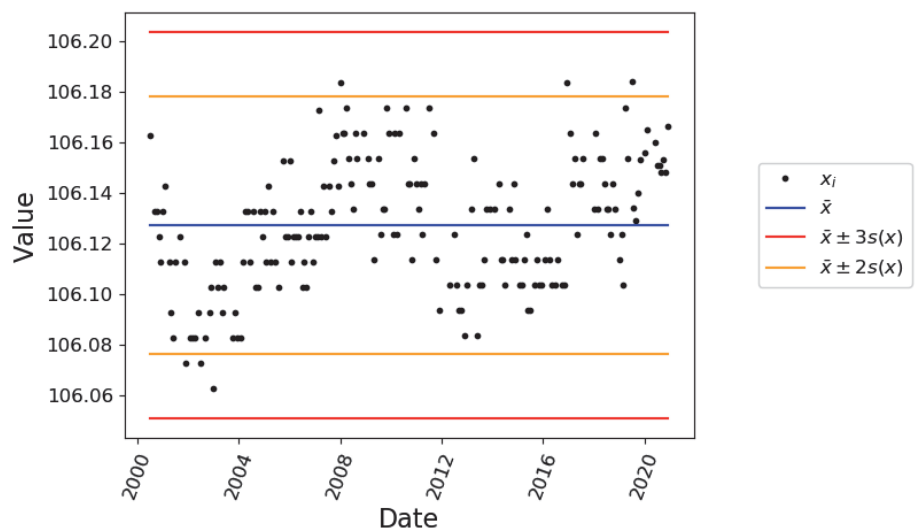


Figure 17.
x-chart of the periodic control of the SIR metrology system.

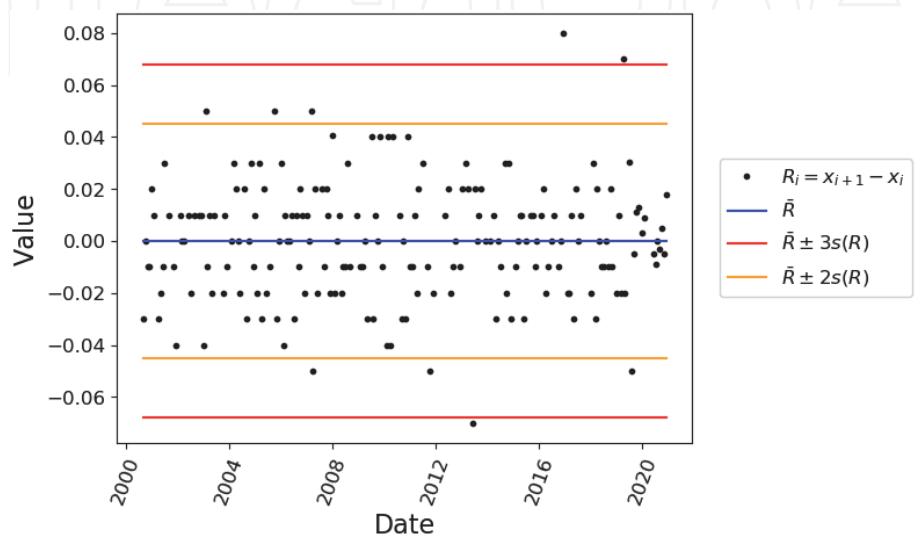


Figure 18.
R-chart of the periodic control of the SIR metrology system.

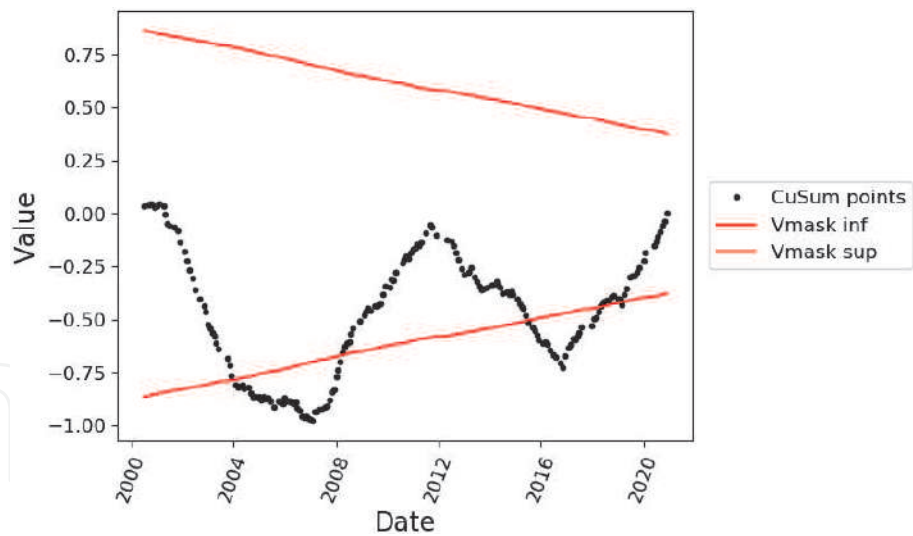


Figure 19.
CUSUM chart of the periodic control of the SIR metrology system.

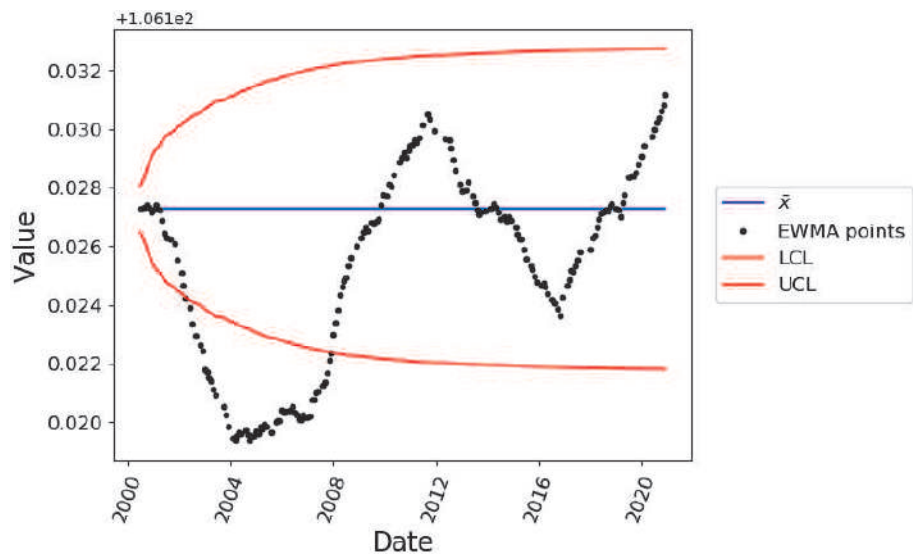


Figure 20.
EWMA chart of the periodic control of the SIR metrology system.

the measurement model for the SIR measurement because the quantity delivered by the system is a ratio of a punctual current measurement (at a time t_i) from which this low-frequency component revealed here is suppressed by the method (Figure 17–20).

We have underlined, through these simulated and real datasets, the limitation of control charts to deal with the evaluation of the long-term stability of metrology instruments. In this case, time series analysis could be used as more appropriate tool to address this objective.

An example of time series analysis is introduced below.

5. Introduction to time series analysis applied to a long-term measurement model

It has been seen that the autocorrelated model introduced in Eq. (10) is appropriate to represent measurement data when observed over a long-term period.

Eq. (10) is here rewritten in a state-space model where the measurement is decomposed by the following:

- the fluctuation of the expectation value $(x_1, \dots, x_i, \dots, x_N)$ with the low-frequency random noise at measurement times $(t_1, \dots, t_i, \dots, t_N)$,
- and the measurements gathered in the vector $(y_1, \dots, y_i, \dots, y_N)$ where the Gaussian white noise is finally added to $(x_1, \dots, x_i, \dots, x_N)$.

The model becomes,

$$\begin{cases} x_i = x_{i-1} + \dot{x}_{i-1} \\ \dot{x}_i = \dot{x}_{i-1} + \delta_i \\ y_i = x_i + \varepsilon_i \end{cases} \quad (12)$$

The drift velocity $\dot{x}_i = x_i - x_{i-1}$ is introduced such that the dynamic Gaussian noise $\delta_i \sim \mathcal{N}(0, \tau^2)$ describes a random walk parametrized by a variance τ^2 . And the measurement noise $\varepsilon_i \sim \mathcal{N}(0, \sigma^2)$ is Gaussian white noise with a variance σ^2 .

The idea behind time series analysis is to deconvolve the low-frequency fluctuation of the expectation values $(x_1, \dots, x_i, \dots, x_N)$ from the observations $(y_1, \dots, y_i, \dots, y_N)$.

At first, the measurement variance σ^2 is evaluated by using the median of all the punctual type A evaluation of the standard deviation $s(y_i)$ which are (by definition) isolated from the dynamic component.

$$\sigma^2 = \text{median}(s^2(y_i)) \quad (13)$$

with,

$$s^2(y_i) = \frac{\sum_{j=1}^M \left(y_i^{(j)} - M^{-1} \sum_{l=1}^M y_i^{(l)} \right)^2}{M-1}. \quad (14)$$

$(y_{N+1}^{(1)}, \dots, y_{N+1}^{(j)}, \dots, y_{N+1}^{(M)})$ is the set of measurements obtained at the time t_i during a period that allowing type A evaluation according to the Gaussian white noise model. Here, control charts can be used to verify this hypothesis.

Eq. (12) is transformed in the following matrix form:

$$\begin{cases} X_i = FX_{i-1} + W_i \\ y_i = HX_i + \varepsilon_i \end{cases} \quad (15)$$

with the “state vector” $X_i = \begin{pmatrix} x_i \\ \dot{x}_i \end{pmatrix}$, the “transition matrix” $F = \begin{pmatrix} 1 & 1 \\ 0 & 1 \end{pmatrix}$, the “dynamic noise matrix” $W_k = \begin{pmatrix} 0 \\ \delta_i \end{pmatrix}$, and the “observation matrix” $H = (1 \ 0)$.

5.1 The Kalman filter

Given the Gaussianity of the noises (both dynamic noise δ_i and measurement noise ε_i) of this linear model (in the sense of time series), the Kalman filter (KF) provides an optimal estimation of the states X_i given the current and past measurements $y_{1:i}$. The optimality of KF to solve Eq. (15) is established through both least-square interpretation and the probabilistic Bayesian analysis [14, 15]. Hence, KF is a

recursive Bayesian filter where the states X_i and the measurements y_i are Markov processes implying

$$\begin{cases} p(X_i|X_{1:i-1}) = p(X_i|X_{i-1}) \\ p(y_i|X_{1:i}) = p(y_i|X_i). \end{cases} \quad (16)$$

KF evaluates, at each time step i , the parameters of the Gaussian posterior distribution $p(X_i|y_{1:i})$ in two steps:

- The first step consists of predicting the state X_i given past measurement data $y_{1:i-1}$. The posterior distribution $p(X_{i-1}|y_{1:i-1})$ at t_{i-1} is used to build a prior distribution at the time t_i according to the linear model (see Eq. (15)) from t_{i-1} to t_i such as

$$p(X_i|y_{i-1}) = \int p(X_i|X_{i-1}) p(X_{i-1}|y_{i-1}) dX_{i-1}. \quad (17)$$

- The second step aims to update the posterior distribution at t_i given the predicted prior $p(X_i|y_{1:i-1})$, and the likelihood $p(y_i|X_i)$ of the measurement y_i given the estimate X_i .

$$p(X_i|y_i) \propto p(X_i|y_{i-1}) p(y_i|X_i). \quad (18)$$

The posterior state estimate $\hat{X}_{i|i}$ and the posterior of the covariance $P_{i|i}$ of the posterior distribution $p(X_i|y_{1:i})$ are evaluated through the Kalman filtering process described below.

From $i = 1$ to $i = N$, KF predicts the state X_i and the measurement y_i at the time step i given the previous state at $i - 1$:

$$\begin{cases} \hat{X}_{i|i-1} = F\hat{X}_{i-1|i-1} \\ \hat{y}_{i|i-1} = H\hat{X}_{i|i-1}. \end{cases} \quad (19)$$

With the state and measurement covariances, P_i and S_i such that:

$$\begin{cases} P_{i|i-1} = FP_{i-1|i-1}F^T + \tau^2 \\ S_i = HP_{i|i-1}H^T + \sigma^2. \end{cases} \quad (20)$$

Then, the pre-fit residual (innovation) e_i of the estimation and the Kalman gain K_i are calculated by

$$\begin{cases} e_i = y_i - \hat{y}_{i|i-1} \\ K_i = P_{i|i-1}H^TS_i^{-1}. \end{cases} \quad (21)$$

Finally, the updated state estimation is

$$\begin{cases} \hat{X}_{i|i} = \hat{X}_{i|i-1} + K_ie_i \\ P_{i|i} = (I - K_iH)P_{i|i-1}, \end{cases} \quad (22)$$

with I : the identity matrix.

5.2 The Rauch-Tung-Striebel smoother

The KF estimates the states $\hat{X}_{i|1:i}$ given present and past observations from t_1 to t_i . To refine the estimation, a KF backward pass (smoothing pass) processes the filtered estimates data from t_N to t_1 . This procedure is called the Rauch-Tung-Striebel smoother (RST) [16, 17]. Symmetrically to the forward KF optimal filter, the optimal smoothing also consists in:

- a prediction step where the state X_{i+1} is estimated given measurement data $y_{1:i}$ and the forecasted state backward transition according to the linear model from t_{i+1} to t_i .

$$p(X_{i+1}|y_{1:i}) = \int p(X_{i+1}|X_i)p(X_i|y_{1:i})dX_i \quad (23)$$

- The second step aims to update the posterior distribution at t_i given all the data $p(X_i|y_{1:N})$.

$$p(X_i|y_{1:N}) = p(X_i|y_{1:i}) \int \frac{p(X_{i+1}|X_i)p(X_{i+1}|y_{1:N})}{p(X_{i+1}|y_{1:i})} dX_{i+1}. \quad (24)$$

The RTS smoother calculates the Maximum A Posteriori (MAP) estimate $\hat{X}_{i|1:N}$ of the posterior probability $p(X_i|y_{1:N})$ given all the observations (past, present, and future) from t_1 to t_N .

From $i = N$ to $i = 1$, the residual e'_i between the filtered state $\hat{x}_{i+1|i}$ and the prediction $\hat{x}_{i+1|1:N}$ is used to calculate a new Kalman gain G_i such as

$$\begin{cases} e'_i = \hat{X}_{i+1|1:N} - \hat{X}_{i+1|i} \\ G_i = P_{i|i+1}F^TP_{i+1|i}^{-1} \end{cases} \quad (25)$$

The optimal state estimation is finally given by

$$\begin{cases} \hat{X}_{i|1:N} = \hat{X}_{i|i} - G_ie'_i \\ P_{i|1:N} = P_{i|i} + G_i(P_{i+1|1:N} - P_{i+1|i})G_i^T \end{cases} \quad (26)$$

5.3 The auto-tuning of the RTS smoother

As the measurement noise variance σ^2 is evaluated, by definition, through measurement repeated during a period free from long-term fluctuation (Eq. (17)), the variance of the dynamic noise τ^2 is the remaining unknown parameter of the model. The auto-tuning procedure proposed here to evaluate τ starts with a loss function L defined by

$$L(\tau) = \sum_{i=2}^N e_i^2 + (\hat{x}_{i|1:N} - \hat{x}_{i-1|1:N})^2. \quad (27)$$

The value $\hat{\tau}$ minimizing $L(\tau)$ aims to minimize the residual between the measurements y_i and the estimations of the measurements $\hat{y}_{i|i-1}$ as well as the distance between two consecutive filtered estimations $\hat{x}_{i|1:N}$ and $\hat{x}_{i-1|1:N}$. On the one hand, if this last smoothing constraint is not considered, τ will diverge toward high values describing a totally unstable system. On the other hand, if the prediction error of

the model is not considered, τ will be canceled by describing a stable system with constant $\hat{x}_{i|i}$ values. So, the loss function of Eq. (27) permits to produce a model of measurement of a controlled process containing a low-frequency dynamic noise. The variance of the low-frequency dynamic noise is determined through an iterative procedure minimizing $L(\tau)$ such that,

$$\hat{\tau} = \underset{\tau}{\operatorname{argmin}}(L(\tau)). \quad (28)$$

The auto-tune RTS smoother provides filtered values $\hat{x}_{i|1:N}$ where the measurement noise, ε_i , is removed given the knowledge of the variances of the measurement noise σ^2 (see Eqs. (13) and (14)) and the dynamic noise $\hat{\tau}^2$. So, the global hidden uncertainty component from the long-term process random noise can be evaluated from the deconvolved data $\hat{x}_{i|1:N}$ such that,

$$s(\hat{x}_{i|1:N}) = (N-1)^{-1} \sum_{i=1}^N \left(\hat{x}_{i|1:N} - N^{-1} \sum_{j=1}^N \hat{x}_{j|1:N} \right)^2. \quad (29)$$

Thanks to the intrinsic unfolding of the measurement noise (Gaussian white) and the process noise (Gaussian red) defined in the dynamic model (Eq. 12), the standard uncertainty $u(x_{N+1})$ of a new measurement at t_{N+1} can be obtained by the quadratic summation of the type A uncertainty evaluation $s(x_{i(N+1)})$ obtained under repeated conditions $(y_{N+1}^{(1)}, \dots, y_{N+1}^{(j)}, \dots, y_{N+1}^{(M)})$ and the type B uncertainty evaluation evaluated using all historical data $(y_1, \dots, y_i, \dots, y_N)$ through the above-described auto-tuned RTS smoother.

Therefore, the standard uncertainty $u^2(x_{N+1})$ of the next measurement at t_{N+1} should be inflated considering the impact of the dynamic noise such that,

$$u^2(x_{T+1}) = s^2(x_{i(T+1)}) + P_{N+1|1:N}(1) \quad (30)$$

With,

$$P_{N+1|1:N} = F P_{N|1:N} F^T + \tau^2 \quad (31)$$

This auto-tuning of a RTS smoother applied to measurement data recorded over a long-term period fully address the recommendation of the JCGM100:2008 guide [4]:

“Because the mathematical model may be incomplete, all relevant quantities should be varied to the fullest practicable extent so that the evaluation of uncertainty can be based as much as possible on observed data. Whenever feasible, the use of empirical models of the measurement founded on long-term quantitative data, and the use of check standards and control charts that can indicate if a measurement is under statistical control, should be part of the effort to obtain reliable evaluations of uncertainty. The mathematical model should always be revised when the observed data, including the result of independent determinations of the same measurand, demonstrate that the model is incomplete. A well-designed experiment can greatly facilitate reliable evaluations of uncertainty and is an important part of the art of measurement.”

6. Application of time series analysis on simulated and real measurement data

The time series analysis through the auto-tuned RST smother is presented in **Figure 21** for the simulated dataset from Section 3.3 obtained with the

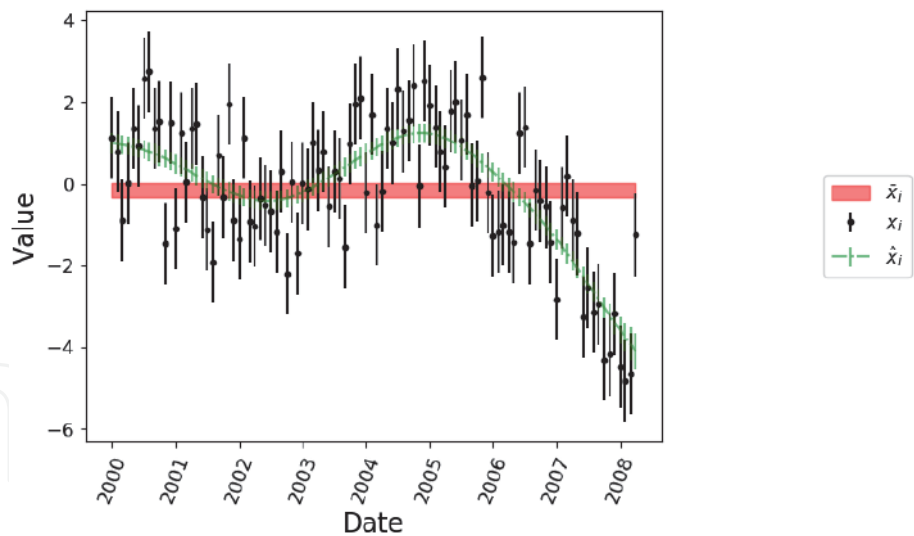


Figure 21.
Time series analysis of the measurement data simulated form the autocorrelated model.

autocorrelated model. Black points are the measurement points y_i with error bars representing the standard deviation $s(y_i)$. Green points are the estimations of the low-frequency fluctuations (red noise) of the measurement \hat{x}_i with error bars representing the standard deviation $s(\hat{x}_i)$. The red line is the global expectation value where the thickness of the line represents ± 1 standard deviation.

It can be seen the good deconvolution of the low-frequency random noise shown in green points. This leads to a standard uncertainty from this autocorrelated noise, $s(\hat{x}_{i1:N}) = 1.31$. This value is significant when compared to type A evaluation of individual measurement points $\sigma^2 = 1.74$.

Also, the time series analysis through the auto-tuned RST smother is presented in **Figure 22** when applied to the periodic control of the SIR metrology system. Again, black points are the measurement points y_i with error bars representing the standard deviation $s(y_i)$. Green points are the estimations of the low-frequency fluctuations (red noise) of the measurement \hat{x}_i with error bars representing the standard deviation $s(\hat{x}_i)$. The red line is the global expectation value where the thickness of the line represents ± 1 standard deviation.

The analysis using control charts (see Section 4.2) has led to conclude that the system is not under statistical control although autocorrelated noise is expected for

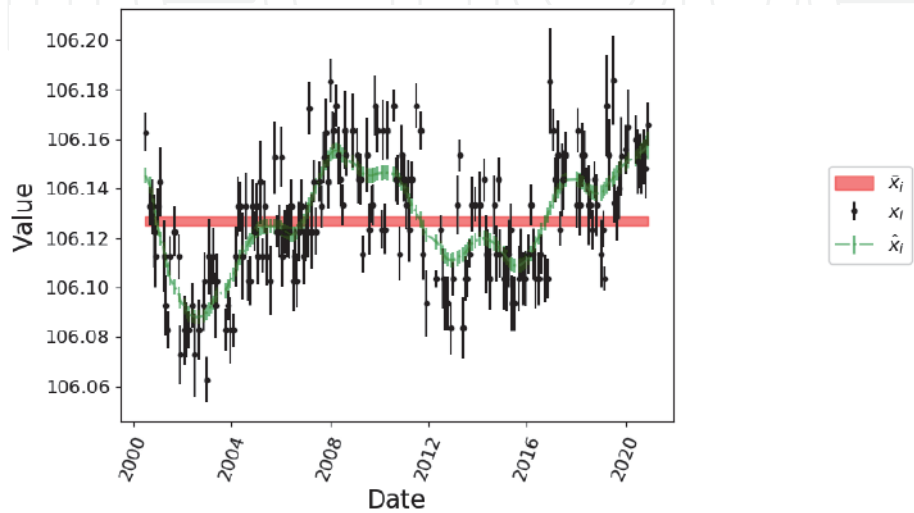


Figure 22.
Time series analysis of the periodic control of the SIR metrology system.

such a long-term period of monitoring. The optimal Bayesian smoother permits to properly deconvolve this component (see green points) and to evaluate the standard uncertainty associated with it: $s(\hat{x}_{i|1:N}) = 0.0183$. This value is significant when compared to type A evaluation of individual measurement points $\sigma^2 = 0.025$.

7. Conclusion

It has been emphasized through simulated and experimental data that control charts (Shewhart, CUSUM, EWMA charts) are convenient tools to assess whether a measurement system is under statistical control or not. They test the compliance of the measured dataset with a Gaussian white noise model. It can notably be used to determine the possibility to apply a type A evaluation of uncertainty on the measurement data.

However, care should be taken when monitoring over long periods of time. A low-frequency random noise will inevitably appear. Despite its stochastic nature, the latter will induce detection by control charts. In this case, it is not appropriate to conclude by a loss of control of the system but rather to re-evaluate the measurement model to include this long-term component. To that end, time series analysis could be implemented to better deal with this particular case of measurement data.


An auto-tuned Rauch-Tung-Striebel smoother, based on the optimal Bayesian filter called Kalman filter, is introduced to illustrate how time series analysis can help to deconvolve the components of the long-term measurement model. The low-frequency random fluctuation (aka red noise) can be estimated and used to evaluate the standard uncertainty component it induces on the measurement.

Author details

Romain Coulon
Bureau International des Poids et Mesures, Pavillon de Breteuil, Sèvres Cedex,
France

*Address all correspondence to: romain.coulon@bipm.org

IntechOpen

© 2021 The Author(s). Licensee IntechOpen. This chapter is distributed under the terms of the Creative Commons Attribution License (<http://creativecommons.org/licenses/by/3.0>), which permits unrestricted use, distribution, and reproduction in any medium, provided the original work is properly cited. 

References

- [1] Milton MJT, Possolo A. Trustworthy data underpin reproducible research. *Nature Physics*. 2020;**6**:117-119
- [2] ISO/IEC 17025:2017 General requirements for the competence of testing and calibration laboratories
- [3] Wikipedia Seven basic tools of quality
- [4] JCGM-BIPM. Evaluation of Measurement Data—Guide to the Expression of Uncertainty in Measurement. Vol. 50. Geneva: International Organization for Standardization; 2008. p. 134
- [5] Anon ISO 7870-1:2019(en) Control charts—Part 1: General guidelines
- [6] Prins JC, Croarkin PT. What are Control Charts? Methods, NIST/SEMATECH E-handb. Stat 6.3.1. Gaithersburg: NIST; 2012
- [7] Leitao S, Emilia M, Pedro J. Applications of control charts ARIMA for autocorrelated data. In: *Practical Concepts of Quality Control*. IntechOpen; 2012
- [8] Bagshaw M, Johnson RA. The effect of serial correlation on the performance of CUSUM tests II. *Technometrics*. 1975;**17**:73
- [9] Tamhane AC, Malthouse EC. Control charts for autocorrelated process data. In: *Advances in Statistical Decision Theory and Applications*. Boston, MA: Birkhäuser Boston; 1997. pp. 371–385
- [10] Umar Farouk A, Mohamad I. The enhanced EWMA control chart with autocorrelation. *Jurnal Teknologi*. 2014;**71**:89-94
- [11] Coulon R, Broda R, Cassette P, Courte S, Jerome S, Judge S, et al. The international reference system for pure β -particle emitting radionuclides: An investigation of the reproducibility of the results. *Metrologia*. 2020;**57**: 035009
- [12] Coulon R, Judge S, Liu H, Michotte C. The international reference system for pure beta-particle emitting radionuclides: an evaluation of the measurement uncertainties. *Metrologia*. 2021;**58**:025007
- [13] Ratel G. The système international de référence and its application in key comparisons. *Metrologia*. 2007;**44**:S7-S16
- [14] Jazwinski A. *Stochastic Processes and Filtering Theory* (Pittsburgh). New York and London: Academic Press; 1970
- [15] Bar-Shalom Y, Li X-R, Kirubarajan T. *Estimation with Applications to Tracking and Navigation*. New York, USA: John Wiley & Sons, Inc.; 2001
- [16] Rauch H. Solutions to the linear smoothing problem. *IEEE Transactions on Automatic Control*. 1963;**8**:371–372
- [17] Rauch HE, Tung F, Striebel CT. Maximum likelihood estimates of linear dynamic systems. *AIAA Journal*. 1965;**3**: 1445–1450

We are IntechOpen, the world's leading publisher of Open Access books Built by scientists, for scientists

6,300

Open access books available

171,000

International authors and editors

190M

Downloads

Our authors are among the

154

Countries delivered to

TOP 1%

most cited scientists

12.2%

Contributors from top 500 universities



WEB OF SCIENCE™

Selection of our books indexed in the Book Citation Index
in Web of Science™ Core Collection (BKCI)

Interested in publishing with us?
Contact book.department@intechopen.com

Numbers displayed above are based on latest data collected.
For more information visit www.intechopen.com



The Data Evaluation of Interlaboratory Comparisons for Calibration Laboratories

Oleh Velychko and Tetyana Gordiyenko

Abstract

National accreditation agencies in different countries have set quite strict requirements for accreditation of testing and calibration laboratories. Interlaboratory comparisons (ILCs) are a form of experimental verification of laboratory activities to determine technical competence in a particular activity. Successful results of conducting ILCs for the laboratory are a confirmation of competence in carrying out certain types of measurements by a specific specialist on specific equipment. To obtain reliable results of ILC accredited laboratories, it is necessary to improve the methods of processing these results. These methods are based on various data processing algorithms. Therefore, it is necessary to choose the most optimal method of processing the obtained data, which would allow to obtain reliable results. In addition, it is necessary to take into account the peculiarities of the calibration laboratories (CLs) when evaluating the results of ILC. Such features are related to the need to provide calibration of measuring instruments for testing laboratories. The evaluation results for ILCs for CLs are presented. The results for all participants of ILCs were evaluated using the E_n and z indexes. The obtained results showed that for the such ILCs it is also necessary to evaluate the data using the z index also.

Keywords: interlaboratory comparison, data evaluation, referent laboratory, calibration laboratory, calibration, measurement uncertainty

1. Introduction

Participants in the International Laboratory Accreditation Cooperation (ILAC) Mutual Recognition Agreement (MRA) recognize the calibration or test results obtained by each other's accredited calibration and testing laboratories [1–4]. ILAC Policy and Procedural publications are for the operation of the ILAC MRA. ILAC has a special policy for participation in proficiency testing activities, on metrological traceability of measurement results, for measurement uncertainty in calibration [5–7]. The policy for measurement uncertainty to base on the Guide to Uncertainty in Measurement (GUM) [8–11] and retains the common understanding of the term calibration and measurement capabilities (CMCs) from the joint declaration issued by the International Bureau of Weights and Measures (BIPM) and ILAC [12]. ILAC has a special guideline for measurement uncertainty in testing [13]. This document provides guidance for the evaluation and reporting of measurement uncertainty in testing accordance with the requirements of the International Standard ISO/IEC 17025 [14].

National accreditation agencies in different countries have set quite strict requirements for accreditation of testing and calibration laboratories. Laboratory accreditation criteria in most accreditation systems include three main groups: laboratory technical equipment, personnel competence, and the effectiveness of the quality system. Interlaboratory comparisons (ILCs) are a form of experimental verification of laboratory activities to determine technical competence in a particular activity. Successful results of conducting ILCs for the laboratory are a confirmation of competence in carrying out certain types of measurements by a specific specialist on specific equipment.

To obtain reliable results of ILC accredited laboratories, it is necessary to improve the methods of processing these results. These methods are based on various data processing algorithms as required by international and regional guidelines and standards. To conduct ILC for CLs, it is necessary to take into account the relevant requirements of the international standards ISO/IEC 17025 [14] and ISO/IEC 17043 [15]. Therefore, it is necessary to choose the most optimal method of processing the obtained data, which would have a minimum number of restrictions on the application and allow to obtain reliable results. In addition, it is necessary to take into account the peculiarities of the calibration laboratories (CLs) when evaluating the results of ILC. Such features are related to the need to provide calibration of measuring instruments for testing laboratories.

ILCs for CLs are held nationally in different countries. Such ILCs are carried out to establish the competence of the CLs in calibrating various measuring instruments and working standards for various measured quantities [16–24]. For their implementation, various calibration objects are used. To evaluate the ILC data, various methods of their data processing are used [25–30], and to estimate the measurement uncertainty, the regional guidance EA-04/02 M [31] is additionally used, in addition to the ILAC documents [8, 13]. However, in addition to the method of data evaluation, it is necessary to take into account other influencing factors on the CL result of ILC. In particular, unsatisfactory ILC results for all participating CLs may be associated with a large time drift of the calibrated measuring instrument.

The growing practical need of ILCs for CLs to ensure recognition of the obtained results at both national and international levels underscores the relevance of this research.

2. The national interlaboratory comparisons for calibration laboratories

The main purpose of accredited CLs is to calibrate working standards and measuring instruments for accredited testing laboratories. Significantly more testing laboratories are accredited by national accreditation bodies than CLs. For example, at the middle of 2021, 837 testing and 35 calibration laboratories were accredited in Ukraine. This represents only 4% of accredited CLs of the total number of all accredited laboratories. Therefore, the number of ILCs for testing laboratories is objectively much larger than for CLs.

The State Enterprise “Ukrmetrteststandard” (Ukraine) as a referent laboratory (RL) organized and carry out seven ILCs for accredited CLs from 2016 to 2019 [32–35, etc]. The list of these ILCs is shown in **Table 1**. The calibration objects for these ILCs were working standards and measuring instruments for electrical quantities, and time and frequency. When carrying out comparisons, CLs calibrated objects in accordance with the requirements of the international standard ISO/IEC 17025 [14]. The total number of calibration object parameters ranged from 3 to 12. The total number of CLs with RL that took part in these comparisons ranged from 5 to 10.

ILC	Calibration object	Number of parameters	Number of participants	Period of carrying out
ILC1	Precision measuring thermocouple	AC voltage at 5 frequencies	5 labs	2016–2018
ILC2	Measures of electrical resistance (1th round)	3 nominations of resistance	8 labs	2016
ILC3	Measures of electrical resistance (2th round)	3 nominations of resistance	5 labs	2018–2019
ILC4	Precision measure of electric power	6 power factors at 2 frequencies	8 labs	2016–2018
ILC5	Low frequency signal generator	AC voltage at one frequency, total harmonic factor at 4 frequencies, 5 frequencies	4 labs	2016
ILC6	Electronic stopwatch	3 time intervals	9 labs	2016
ILC7	High-frequency signal generator	3 frequencies	10 labs	2018

Table 1.
The list of national ILCs for CLs.

In all presented ILCs, the assigned value (AV) with its uncertainty was taken as the value with its uncertainty of the RL. This was done because the RL had the best measurement capabilities among all CLs that took part in the comparisons. For many years RL has taken part in international comparisons of national measurement standards of electrical quantities within the framework of Regional Metrological Organizations (COOMET, EURAMET, and GULFMET) and had positive results. RL also had published CMCs for some electrical quantities in the BIPM Key Comparison Database [36].

A program for all ILCs was implemented in accordance with the requirements of ISO/IEC 17043 [15]. CLs that participated in the ILCs performed calibration of the measuring instruments (calibration object) provided to the RL in accordance with their own methods according to the radial scheme [4]. RL sent the calibration object to the participating laboratory, and this laboratory returned this object back to RL. In this case, the RL constantly monitored the stability of the calibration object [35, 37]. The RL determined the characteristics of the instability of the calibration object before and after its research in the CLs participating in the ILC.

In accordance with the adopted ILC programs, RL analyzed the calibration data provided by the CLs [38], in particular, analyzed the declared measurement uncertainty. The data obtained from CLs were necessarily checked by RL for their consistency. Indicators for assessing of consistency were E_n and z indexes set and defined in [4, 15]. The general algorithm of processing of the received primary data of ILCs given in [34] was used. In case of inconsistent data, RL reported this appropriate CL and analyzed the responses received from this laboratory. RL prepared a report on the comparisons, evaluating the data of all CLs. In the event that the laboratory or laboratories received inconsistent results of comparisons, RL suggested that they take the necessary corrective action.

3. The traditional data evaluation of interlaboratory comparisons

The traditional assessment of ILC data for CLs is carried out in accordance with the requirements of ISO/IEC 17043 [15]. During of the evaluation of primary data

from the participating CLs, the interlaboratory deviation of the measurement results or degree of equivalences (DoE) was calculated based on the ILCs results. The DoE for j -th CLs participant of ILC is calculated using Equation [4, 34, 38].

$$D_{labj} = x_{labj} - X_{AV}, \tag{1}$$

where x_{labj} is measured value for i -th CL; X_{AV} is AV for ILC.

Expanded uncertainty of the result of each participant $U(x_{labj})$ and expanded uncertainty of AV $U(X_{AV})$ were used to check the consistency of the primary ILC data and to calculate E_n index (E_n number) using equation

$$E_n = D_{labj} / \sqrt{U^2(x_{labj}) + U^2(X_{AV})}. \tag{2}$$

$|E_n| \leq 1.0$ indicates satisfactory performance and $|E_n| > 1.0$ indicates unsatisfactory performance [4, 15].

On **Figures 1–3** show the traditional graphical interpretation of the results of three ILCs at one of the calibration points (ILC 2–1, **Figure 1**, ILC 4–2, **Figure 2** and ILC 6–1, **Figure 3** respectively). The evaluation of primary data of all ILCs is carried out by means of the specially developed software “Interlaboratory comparisons” (Ukraine) which implements the algorithm presented in [34]. To prepare reports on ILCs, RL used specified software that allowed calculating the E_n and z indexes and constructing a graphical display of the results. The figures show the DoE with expanded uncertainty for all participating CLs in ILCs. The green dashed line shows the measurement uncertainty limits of the AV of ILC.

Only two laboratories (lab 4 and lab 6 for ILC 2–1) have an unsatisfactory result for two ILCs using the E_n index. E_n index more characterizes the reliability of measurement results of laboratories participating in the ILC, but is not always sufficient to determine the accuracy of measurement results.

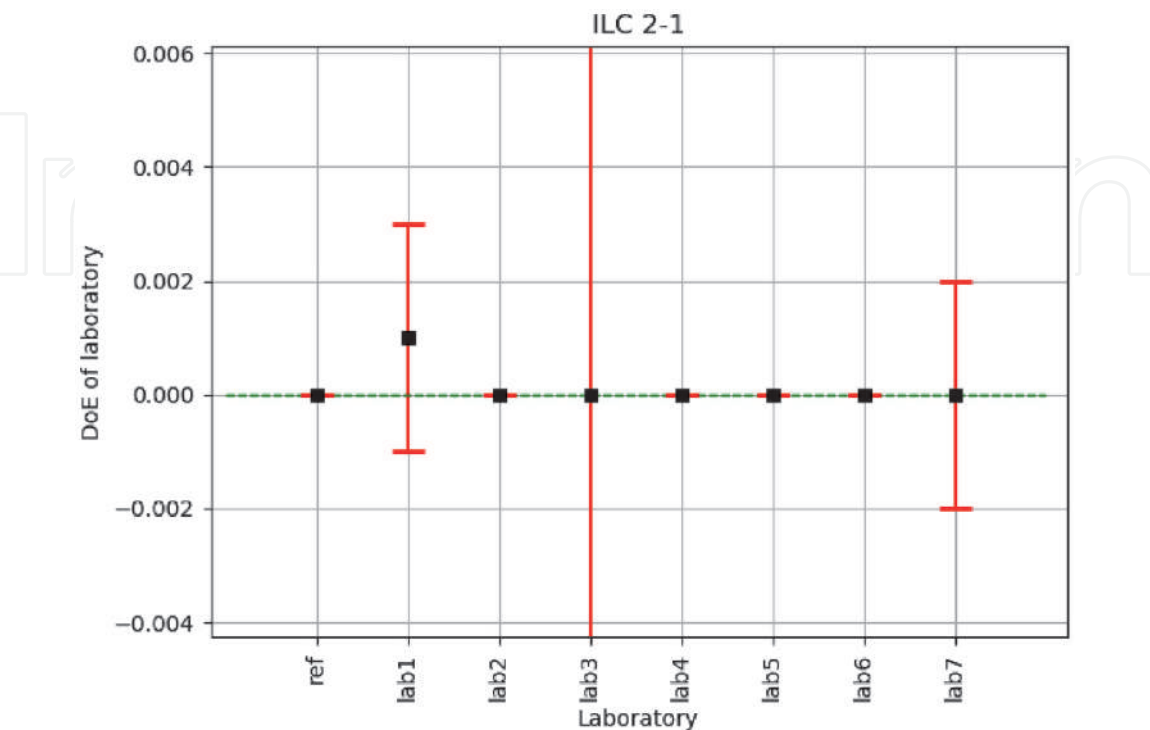


Figure 1.
DoE of CLs for ILC 2–1.

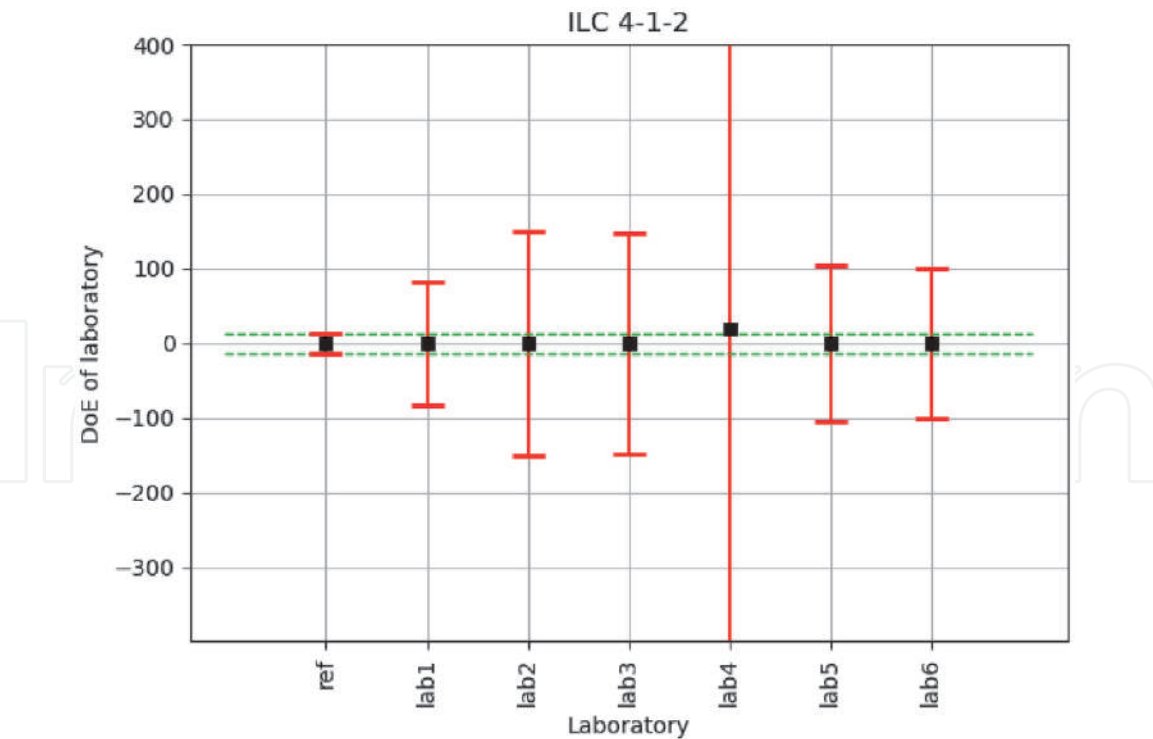


Figure 2.
DoE of CLs for ILC 4-2.

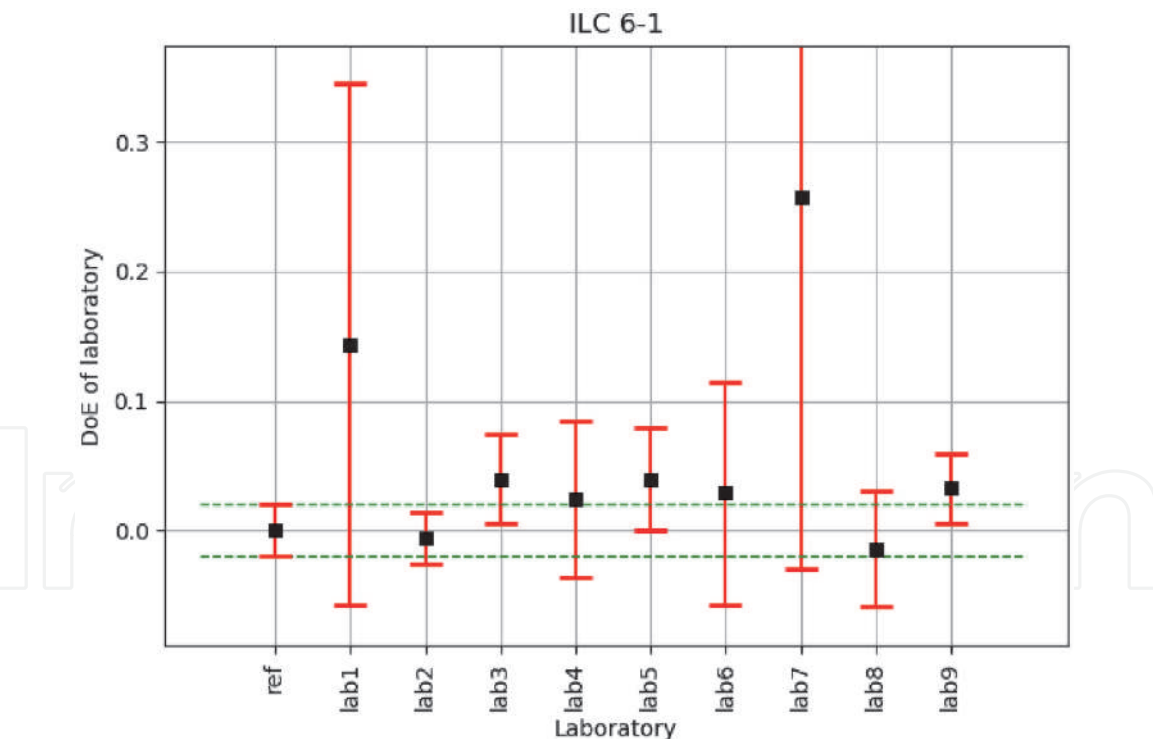


Figure 3.
DoE of CLs for ILC 6-1.

4. The additional data evaluation of interlaboratory comparisons

The consistency evaluation of data using E_n and z indicators is important not only to confirm the technical competence of laboratories participating in the ILC. This will also help to increase the accuracy of calibration by the laboratory participating in the ILC with a corresponding reduction in measurement uncertainty.

The z index compares the measurement results of all laboratories with each other and gives better information about the accuracy of measurements in laboratory. The measurement accuracy is an important characteristic for CL, therefore this index is more suitable for evaluating ILC data for CLs.

z index (z score) is calculated by the equation

$$z = D_{labj} / \sigma, \tag{3}$$

where σ is the standard deviation for qualification assessment (ILC).

$|z| \leq 2.0$ indicates a satisfactory performance characteristic and does not require adjustment or response measures, $2.0 < |z| < 3.0$ indicates a dubious performance characteristic and requires precautionary measures, and $|z| \geq 3.0$ indicates an unsatisfactory performance characteristic and requires adjustment or response measures.

In **Tables 2–8** shows the calculated results of E_n and z indexes at all points of the calibration for all ILCs. E_n and z indexes are zero for RL. Cells with unsatisfactory results are highlighted in grey in the tables. An unsatisfactory result is the excess for E_n index of the value 1, and for the z index of 2 (does not require adjustment or response measures) or 3 (requires adjustment or response measures) [4, 15].

ILC data	Index	Lab 1	Lab 2	Lab 3	Lab 4
ILC1-1	E_n	−0.854	0.444	0.438	−0.312
	z	−0.584	0.114	0.224	−2.462
ILC1-2	E_n	−0.451	0.818	1.522	−0.064
	z	−1.146	0.266	0.605	−2.090
ILC1-3	E_n	−0.645	0.882	0.987	0.022
	z	−1.167	0.483	0.781	1.895
ILC1-4	E_n	−0.147	0.238	0.129	0.452
	z	−0.025	0.019	0.018	2.503
ILC1-5	E_n	—	0.753	0.382	—
	z	—	2.265	1.939	—

Table 2.
Results of ILCs for calibration of precision measuring thermocouple.

ILC data	Index	Lab 1	Lab 2	Lab 3	Lab 4	Lab 5	Lab 6	Lab 7
ILC2-1	E_n	0.249	−0.245	−0.008	−4.631	−0.100	2.352	−0.021
	z	2.677	−0.027	−0.996	−0.208	−0.005	0.188	−0.169
ILC2-2	E_n	−1.955	6.066	−0.018	−0.814	0.256	−0.646	−0.032
	z	−2.404	0.880	−1.460	−0.197	0.056	−0.253	−1.460
ILC2-3	E_n	−0.899	4.179	−0.086	0.171	−0.470	0.975	−0.058
	z	−2.251	1.318	−0.969	0.051	−0.127	0.367	−0.969

Table 3.
Results of ILCs for calibration of measures of electrical resistance (1-th round).

On **Figure 4** shows the graphical interpretation of the results of estimation of E_n (a) and z (b) indexes for ILC 2–1, on **Figure 5** – for ILC 4–2, and in **Figure 6** – for ILC 6–1, respectively.

ILC data	Index	Lab 1	Lab 2	Lab 3	Lab 4
ILC3–1	E_n	0.301	0.133	0.367	0.322
	z	0.117	2.658	0.152	0.961
ILC3–2	E_n	0.194	0.065	0.042	0.051
	z	0.012	2.579	0.004	0.457
ILC3–3	E_n	0.301	0.133	0.367	0.322
	z	0.117	2.658	0.152	0.961

Table 4.
Results of ILCs for calibration of measures of electrical resistance (2-th round).

ILC data	Index	Lab 1	Lab 2	Lab 3	Lab 4	Lab 5	Lab 6
ILC4–1	E_n	0.000	0.004	0.001	−0.013	0.000	0.000
	z	0.002	0.215	0.029	−2.804	0.018	0.018
ILC4–2	E_n	0.000	0.002	0.002	0.034	0.000	0.000
	z	0.001	0.046	0.046	2.875	0.004	0.006
ILC4–3	E_n	0.000	0.002	0.001	0.000	0.000	0.000
	z	0.157	2.683	0.679	−0.192	−0.105	0.157
ILC4–4	E_n	0.000	0.002	0.001	0.000	0.000	0.000
	z	0.207	2.657	1.055	−0.170	−0.075	0.207
ILC4–5	E_n	0.000	0.002	−0.001	0.119	0.000	0.000
	z	0.001	0.013	−0.009	2.859	0.000	0.001
ILC4–6	E_n	0.000	0.002	0.002	0.137	0.000	0.000
	z	0.000	0.012	0.012	2.862	0.000	0.001
ILC4–7	E_n	0.000	0.003	0.003	0.000	0.000	0.000
	z	−0.043	2.260	1.919	−0.043	0.000	−0.043
ILC4–8	E_n	0.000	0.001	0.001	0.000	0.000	0.000
	z	0.176	2.439	2.187	0.176	0.553	0.176
ILC4–9	E_n	0.001	0.002	0.000	0.000	0.000	0.001
	z	0.532	2.787	0.622	−0.009	−0.099	0.532
ILC4–10	E_n	0.000	0.002	0.000	0.000	−0.001	0.000
	z	0.108	2.570	0.569	−0.277	−0.354	0.108
ILC4–11	E_n	0.001	0.002	0.002	0.000	0.000	0.001
	z	0.331	2.462	2.068	0.095	0.253	0.331
ILC4–12	E_n	0.001	0.002	0.001	0.000	0.000	0.001
	z	0.498	2.989	1.329	0.406	0.406	0.498

Table 5.
Results of ILCs for calibration of precision measure of electric power.

ILC data	Index	Lab 1	Lab 2	Lab 3
ILC5-1	E_n	-0.235	-0.014	-0.305
	z	-2.479	-0.077	-1.044
ILC5-2	E_n	-0.050	-0.056	0.036
	z	-1.095	-1.461	1.095
ILC5-3	E_n	0.040	0.000	0.035
	z	1.206	0.000	2.412
ILC5-4	E_n	0.074	0.033	0.068
	z	1.414	1.414	2.828
ILC5-5	E_n	0.737	0.397	0.139
	z	2.399	2.181	0.727
ILC5-6	E_n	-0.087	-0.055	-0.016
	z	-2.557	-1.627	-0.465
ILC5-7	E_n	0.289	0.278	0.122
	z	2.448	2.292	1.011
ILC5-8	E_n	-0.086	0.016	-3.258
	z	-0.063	0.012	-2.326
ILC5-9	E_n	-0.284	-0.061	0.029
	z	-2.315	-0.489	0.233
ILC5-10	E_n	-0.947	-1.024	0.692
	z	-1.335	-1.442	0.975

Table 6.
Results of ILCs for calibration of low frequency signal generator.

ILC data	Index	Lab 1	Lab 2	Lab 3	Lab 4	Lab 5	Lab 6	Lab 7	Lab 8	Lab 9
ILC6-1	E_n	0.713	-0.212	0.992	0.379	0.894	0.328	0.897	-0.290	0.982
	z	1.811	-0.075	0.503	0.302	0.503	0.365	3.245	-0.176	0.415
ILC6-2	E_n	0.998	-0.943	0.733	0.218	0.676	0.161	0.192	-0.379	0.914
	z	3.160	-0.334	0.486	0.729	0.790	0.501	1.686	-0.273	1.413
ILC6-3	E_n	0.711	-0.587	0.459	0.157	0.296	0.065	0.804	-0.273	0.754
	z	2.008	-0.193	0.468	0.908	0.468	0.289	3.012	-0.165	1.582

Table 7.
Results of ILCs for calibration of electronic stopwatch.

ILC data	Index	Lab 1	Lab 2	Lab 3	Lab 4	Lab 5	Lab 6	Lab 7	Lab 8	Lab 9	Lab 10
ILC7-1	E_n	0.050	0.662	-0.072	-0.025	0.643	-0.164	-0.384	-0.039	-0.012	-0.124
	z	1.243	2.666	-0.687	-0.634	0.857	-0.124	-0.588	-0.631	-0.118	-0.433
ILC7-2	E_n	0.067	0.912	-0.076	-0.034	0.775	-0.253	-0.475	-0.068	0.005	-0.052
	z	1.261	2.533	-0.695	-0.629	0.761	-0.182	-0.725	-1.040	0.034	-0.145
ILC7-3	E_n	0.062	1.134	-0.072	-0.053	0.164	-0.160	-0.648	-0.042	-0.014	-0.104
	z	1.045	2.847	-0.746	-0.834	0.164	-0.131	-0.574	-0.427	-0.09	-0.276

Table 8.
Results of ILCs for calibration of high-frequency signal generator.

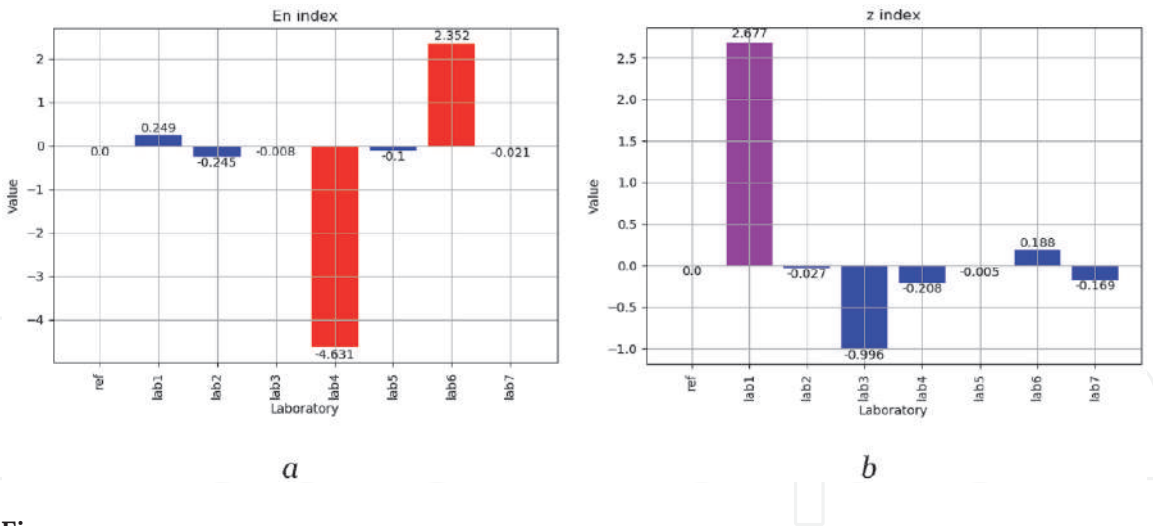


Figure 4.
Values of E_n and z indexes for ILC 2-1: a is E_n index, b is z index.

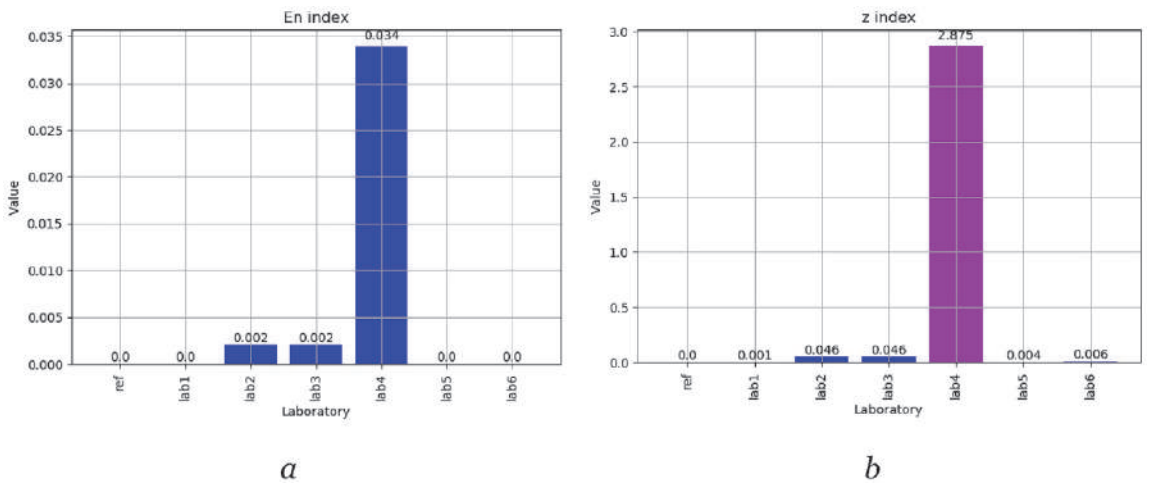


Figure 5.
Values of E_n and z indexes for ILC 4-2: a is E_n index, b is z index.

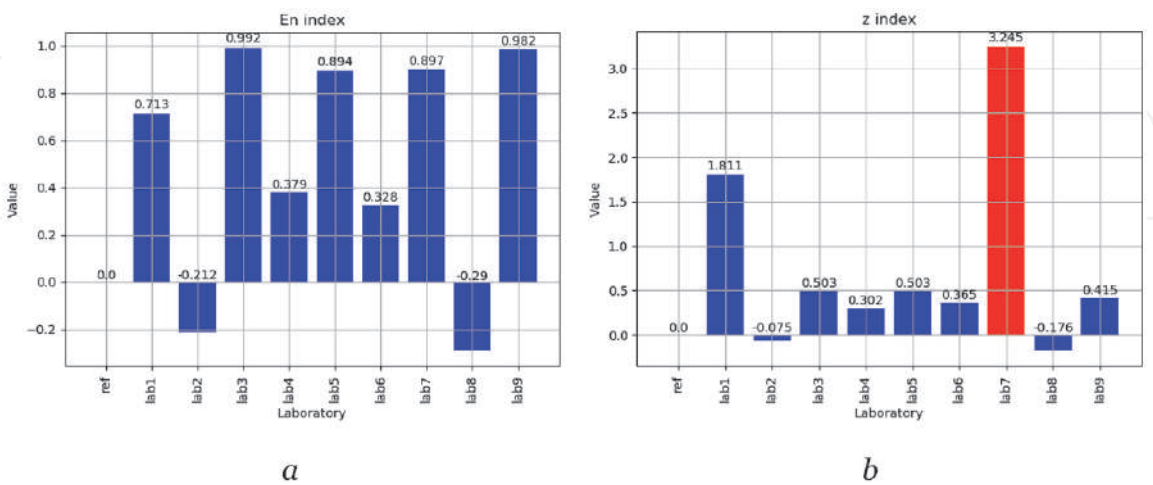


Figure 6.
Values of E_n and z indexes for ILC 6-1: a is E_n index, b is z index.

5. The summarized results of interlaboratory comparisons

The summarized results of estimation of E_n and z indexes for all ILCs are shown in Table 9 and Figure 7. The percentage of discrepancies two assessments for ILCs

ILC	Number of participants*	Number of parameters	$E_n > 1$ for lab	$z > 3$ for lab	$z > 2$ for lab	Percentage of discrepancies in evaluation
ILC1	4 labs	20 points	1 point (5%)	0 point (0%)	4 points (20%)	100%
ILC2	7 labs	21 points	5 points (24%)	0 point (0%)	3 points (14%)	95%
ILC3	4 labs	12 points	0 point (0%)	0 point (0%)	3 points (25%)	100%
ILC4	6 labs	72 points	0 point (0%)	0 point (0%)	14 points (19%)	100%
ILC5	3 labs	30 points	2 points (7%)	0 point (0%)	10 points (33%)	97%
ILC6	9 labs	27 points	0 point (0%)	3 points (11%)	1 point (4%)	100%
ILC7	10 labs	30 points	1 point (3%)	0 point (0%)	3 points (10%)	97%
Total:		212 points	8 points (4%)	3 points (1,4%)	38 points (18%)	—

*Without RL.

Table 9.
The summarized results of estimation of E_n and z indexes for all ILCs.

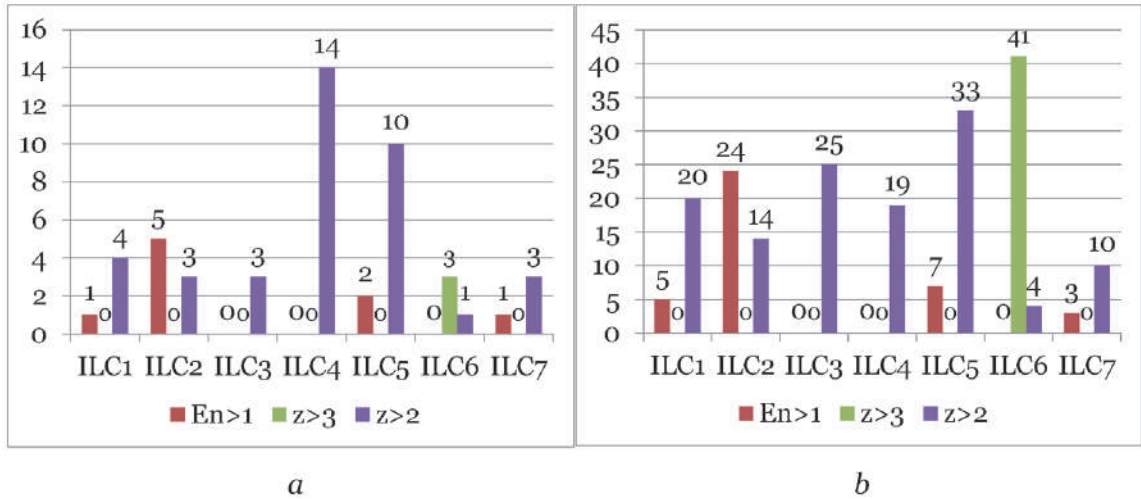


Figure 7.
The summarized results of estimation of E_n and z indexes for all ILCs: a is absolute value, b is percentage value (%).

1, 3, 4 and 6 estimates are 100, for ILCs 2, 5 and 7 estimates are from 95 to 97. This suggests that the conclusions that can be drawn about the technical competence of the laboratories participating in these ILCs are completely inconsistent.

Only one result of ILC1 according to E_n index have inconsistency (lab 3). At the same time, 4 results of ILC1 according to z indexes have inconsistencies (lab 2 and lab 4).

5 results of ILC2 according to E_n indexes have inconsistencies (for labs 1, 2, 4 and 6). At the same time, 3 results of ILC2 according to z indexes have inconsistencies (only for lab 1).

ILC3, ILC4, and ILC6 according to E_n index have no inconsistencies. At the same time, 3 results of ILC3 according to z indexes have inconsistencies (only for lab 2), 14 results of ILC4 according to z indexes have inconsistencies (for labs 2, 3 and 4), and 4 results of the ILC6 according to z indexes have inconsistencies (for labs 2, 3, and 4), including 3 from 4 are very large ($z > 3.0$).

Only one ILC7 result according to E_n index have inconsistency (for lab 2). At the same time, 3 results of the ILC7 according to z indexes have inconsistencies (for lab 2 also).

The results of the data consistency analysis show that all ILCs, taking into account both indexes, have measurement points with unsatisfactory results. Analysis of the data taking into account the E_n index shows that only three ILCs (ILC3, ILC4, and ILC6) have satisfactory results. At the same time, analysis of the data taking into account the z index ($z > 2$) shows that all ILCs have measurement points with unsatisfactory results. ILC6 has measurement points with significantly unsatisfactory results, taking into account the z index ($z > 3$).

If we return to the analysis of **Figures 1–3**, it can be seen that lab 4 for ILCs 2–1 and lab 1 and lab 7 for ILC6–1 have very large declared measurement uncertainties with large DoEs. This led to unsatisfactory results, taking into account the z index. The main reason for the unsatisfactory result of lab 3 for ILCs 1–2, taking into account E_n index, is, on the contrary, a very small declared measurement uncertainty.

The general recommendation for lab 3 and lab 4 for ILC1–2, as well as for lab 4 for ILC4–2, and lab 1 and lab 7 for ILC6–1 is to revise the estimate of the measurement uncertainty, taking into account guides [8, 31]. This measurement uncertainty can be influenced by both the calibration results of the laboratory working standards and the level of competence of the laboratory personnel. Taking these recommendations into account can improve the results of that laboratories participation in other rounds of ILCs or new ILCs.

6. The influence of travelling standards instability

The travelling standards instability can affect the results of ILCs for CLs. Some works are devoted to assessing its influence, in particular compensation for its instability. The repeatability of a good measuring instrument is below 10% of its maximum error as shown in [39]. The travelling standard with 0,2% shows variations of random errors below $\tilde{x} \pm 0.02\%$ where \tilde{x} is the average of the readings during calibration. This a small Type A uncertainty in relation to other components is show.

Typically, RL already takes into account the travelling standards instability in the ILC assigned value X_{AV} and its expanded uncertainty [4].

$$U(X_{AV}) = 2 \cdot \sqrt{u^2(x_{ref}) + u^2(x_{inst})}, \quad (4)$$

where $u(x_{ref})$ is the standard measurement uncertainty obtained by calibrating of travelling standard with a RL; $u(x_{inst})$ is the standard measurement uncertainty from the travelling standard instability of during ILC period

$$u(x_{inst}) = \Delta X_{\max} / \sqrt{3}, \quad (5)$$

ΔX_{\max} is the maximum change in nominal value of travelling standard during ILC period.

The absence of a significant effect of the travelling standards instability on the evaluation of the CL result in the ILC can be at its maximum instability, which is determined by the expression [39].

$$x_{inst} \leq \sqrt{U^2(x_{labj}) + U^2(X_{AV})}. \quad (6)$$

The value of the travelling standards instability can be obtained for several cases: measurements of the RL of the travelling standard in the process of carry out of ILC;

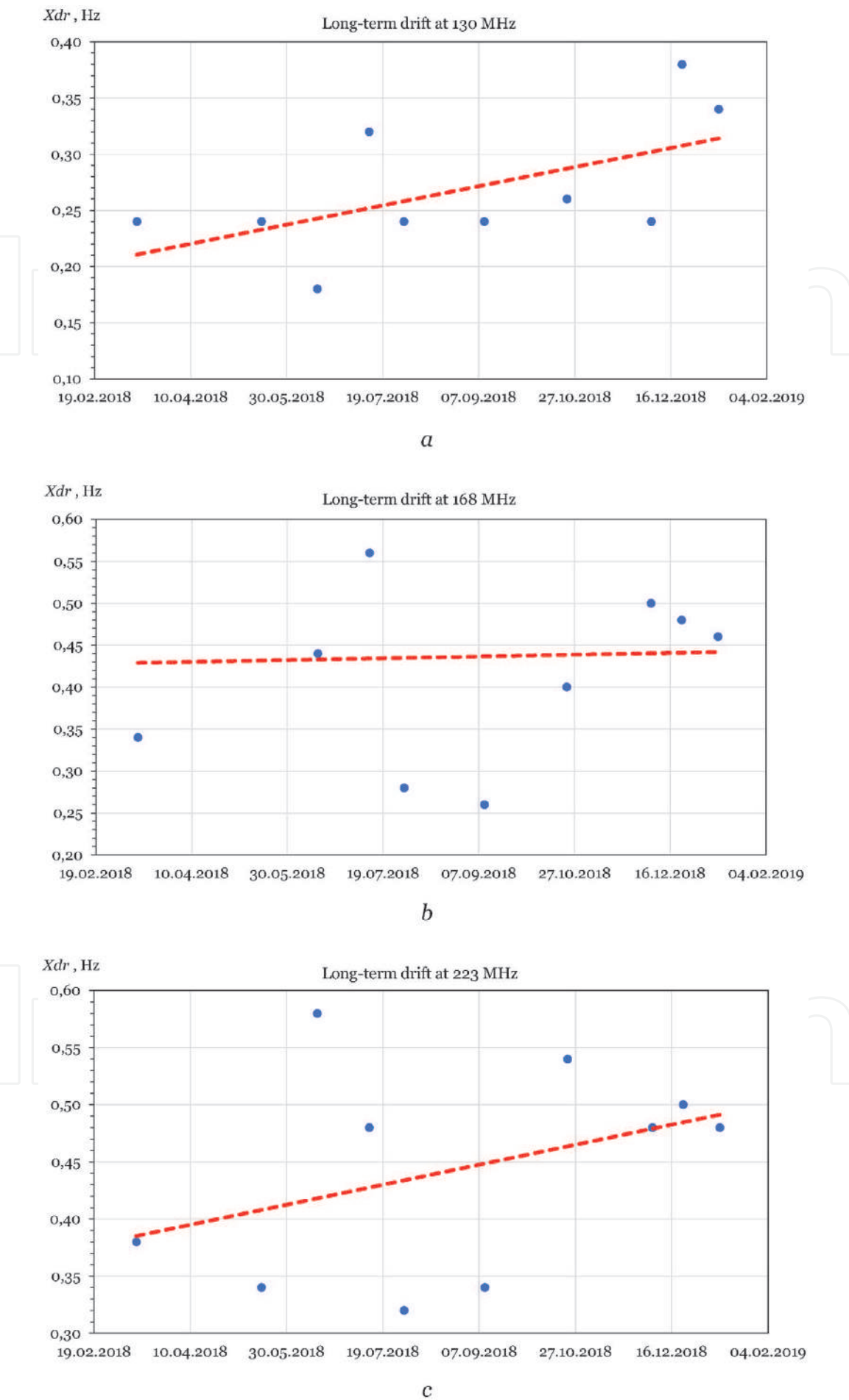


Figure 8.
The drift of travelling standard for ILC7: *a* is frequency 130 MHz, *b* is frequency 168 MHz, *c* is frequency 223 MHz.

from the technical specification for the travelling standard, measurements of the RL of the travelling standard for a long time, and etc. Results of calculating the E_n index for various options for accounting for travelling standards instability are shows in [39].

In any case, from expression (4) it follows that with an increase in the value of the measurement uncertainty associated with instability, the value of the E_n index only decreases. In this case, it can be stated that the use of a more unstable travelling standard can improve the consistency of the ILC data, which is not acceptable for CL. To carry out ILCs for CLs, it is more preferable to use working standards as calibration objects. Typically, a working standard has less instability than a measuring instrument. The use of a measuring instrument as a travelling standard can lead to somewhat distorted results of such ILCs.

An analysis RL of the travelling standard instability for all calibration points of the ILC7 is given in [33]. The drift of travelling standard for ILC7 at all frequencies is presented on **Figure 8**. The uncertainty of travelling standards instability for ILC7 is presented in **Table 10**. The contribution of the uncertainty from the long-term drift of the travelling standard to the standard uncertainty of AV for the entire duration of ILC7 is from 5.3 to 8.3% for all calibration points. Such a drift of the measuring instrument used as a calibration object is acceptable for the ILC. It does not distort the ILC results for the participating CLs.

The list of travelling standard for all ILCs and values of E_n and z indexes are shown in **Table 11**.

The use of a measuring instrument as a calibration object leads to a slight increase in the values of the z index and practically does not affect the E_n index, as can be seen from **Table 11**.

ILC7 point	Frequency (MHz)	$u(X_{AV})$ (Hz)	$u(x_{inst})$ (Hz)	Drift contribution to uncertainty AV (%)
ILC7-1	130	0.12	0.01	8.3
ILC7-2	168	0.17	0.01	5.9
ILC7-3	223	0.19	0.01	5.3

Table 10.
The uncertainty of travelling standards instability for ILC7.

ILC	Calibration object	Working standard	Measuring instrument	E_n index	z index
				Unsatisfactory (%)	
ILC1	Precision measuring thermocouple	Yes	No	5	20
ILC2	Measures of electrical resistance (1th round)	Yes	No	24	14
ILC3	Measures of electrical resistance (2th round)	Yes	No	0	25
ILC4	Precision measure of electric power	Yes	No	0	19
ILC5	Low frequency signal generator	No	Yes	7	33
ILC6	Electronic stopwatch	No	Yes	0	45
ILC7	High-frequency signal generator	No	Yes	3	13

Table 11.
The list of travelling standard for ILCs and values of E_n and z indexes.

7. The improvement of the evaluation of interlaboratory comparison results

Statistical methods for use in proficiency testing by ILCs are presented in [26, 27]. The aim of creating alternative statistics in order to improve the analysis and evaluation of ILC measurement results is research work [40]. The improvement of statistical indicators is proposed by addressing two specific issues: robustness and reliability. The proposed methodology is not traditional for ILC, but it can be used as an additional methodology for checking the results of ILC.

The following conditions are provided for data evaluation of international comparison of national standards: the travelling measurement standard is stable, the measurement results presented by laboratories are reciprocally independent, and the Gaussian distribution is assigned to a measurand in each laboratory [41–44]. The same conditions can be extended for data evaluation of ILCs for CLs. Frequently the measurement procedures for supplementary comparisons of national standards [44] are the calibration procedures of these laboratories. Such calibration procedures can also be extended to ILCs for CLs. In such a case, the calibration capabilities of the laboratory can be confirmed.

The application of z index for evaluation of CL results recommended instead of E_n index since this number is not applicable due to the difficulty in determining the AV [16]. Of course, for accredited test laboratories, it is preferable to use the services of a CL with the best calibration capabilities. Better calibration capabilities of laboratories are characterized by lower calibration uncertainties of working standards and measuring instruments. CLs with a satisfactory value of the E_n index in the ILC, but having large calibration uncertainties become uncompetitive. If we return to the analysis of **Figures 1–3**, it can be seen that lab 1, 3 and 7 for ILCs 1–2, lab 4 for ILC4–2, and lab 1 and lab 7 for ILC6–1 have very large declared measurement uncertainties.

The declared measurement uncertainties of CL for ILC are judged as confirmed if the following equation is satisfied [4, 43].

$$|D_{labj}| < 2u(D_{labj}). \quad (7)$$

In case the declared uncertainties CL don't confirmed during the ILC and for their confirmation it is necessary to participate in other similar ILCs.

Often, a national metrological institute or an accredited CL, which is an RL in ILC, performs high-precision calibration of working standards and measuring instruments for CLs participating in this ILC. In this case, a correlation of the obtained CL results is formed, which must be taken into account when evaluating the data of such an ILC. Covariance's are estimated by careful analysis of the uncertainty budget of CLs by the RL

$$\text{cov}(x_{labj}, X_{AV}) = u_0^2, \quad (8)$$

where u_0^2 is common input to the uncertainty budgets of both results [43].

In this case, the value of the E_n index is calculated by the formula:

$$E_n = D_{labj} / \sqrt{U^2(x_{labj}) + U^2(X_{AV}) - 2\text{cov}(x_{labj}, X_{AV})}. \quad (9)$$

If the value of the E_n index meets the specified requirement (≤ 1.0), then the minimum standard measurement uncertainty, that can be claimed as calibration capability of CL participating in ILC, is:

$$u_{CC}(x_{labj}) = u_{ILC}(x_{labj}). \quad (10)$$

If the value of the E_n index not meets the specified requirement (> 1.0), then the minimum standard measurement uncertainty, that can be claimed as calibration capability of CL participating in ILC, is:

$$u_{CC}(x_{labj}) = \sqrt{\frac{D_{labj}^2}{4} + u^2(X_{AV})}, \quad (11)$$

where $u(X_{AV})$ is the standard measurement uncertainty of AV.

Correspondingly, the extended uncertainty is $U_{0.95}(x_{labj}) = 2u_{ILC}(x_{labj})$.

The same requirements can be extended for compliance (≤ 2.0) or inconsistency (> 2.0) of the value of the z index with the established requirements. In this case, the minimum standard measurement uncertainty, that can be claimed as calibration capability of CL participating in ILC, will be determined by formulas (10) and (11), respectively.

If the standard uncertainty $u(X_{AV})$ of the AV is too large in comparison with the standard deviation σ for ILC, then there is a risk that some laboratories will receive action and warning signals because of inaccuracy in the determination of the AV, not because of any cause within the laboratories. If

$$u(X_{AV}) \leq 0.3\sigma \quad (12)$$

then the uncertainty of the AV is negligible and need not be included in the interpretation of the ILC results. Further, all CLs participating in ILC shall carry out the same number of replicate measurements. This approach assumes that CLs have generally similar repeatability [26].

To evaluate the ILC data, can use z' index also [26] which calculated by the equation

$$z' = D_{labj} / \sqrt{\sigma^2 + u^2(X_{AV})} \quad (13)$$

This equation may be used when the AV is not calculated using the results reported by CLs participating in ILC. z' index shall be interpreted in the same way as z index and using the same critical values of 2.0 and 3.0.

Comparison of the equations for z and z' indexes shows that z' index for ILC will all be smaller than the corresponding z index by a constant factor of $\sigma / \sqrt{\sigma^2 + u^2(X_{AV})}$.

When the inequality established by expression (12) is satisfied, then this factor will fall in the range: $0.96 \leq \sigma / \sqrt{\sigma^2 + u^2(X_{AV})} \leq 1.00$. In this case, z' index will be nearly identical to z index, and it may be concluded that the uncertainty of the AV is negligible. When the inequality established by expression (12) is not satisfied, the difference in magnitude of the z' and z indexes may be such that some z index exceeds the critical values of 2.0 or 3.0.

8. Conclusions

To perform an ILC for CLs, RL must provide a stable working standard or measuring instrument as a calibration object and monitor its drift throughout the ILC. The use of a measuring instrument as a calibration object leads to a slight increase in the values of the z index and practically does not affect the E_n index. The

application of z index for evaluation of CL results recommended instead of E_n index.

The analysis of the results of the ILC for CLs for consistency should include not only the analysis of the values of the E_n index, but also the z index. If we restrict ourselves to only the E_n index, then it is possible to get unreliable results of the ILC and not identify problems in the CL-participants of the ILC. In 3 from 7 ILCs examined, the E_n index showed completely satisfactory results, while the z index in all of these 3 ILCs revealed problematic results from the participating laboratories.

The stable travelling standard, the independent measurement results of laboratories with Gaussian distribution are main conditions for data evaluation of ILC for CLs. To participate in the ILC when declaring its measurement uncertainty, CLs must conduct a thorough analysis of the components of this uncertainty. It is necessary to take into account the correlation of the laboratory data of the participants of the ILC when evaluating its results. Covariance is estimated by carefully analyzing the CL uncertainty budget using RL.

The minimum standard measurement uncertainty that can be claimed as the calibration capability of a CL participating in an ILC can be determined in different ways depending on the value of the obtained E_n index or z index. If the standard uncertainty of AV is too large compared to the standard deviation for the ILC, there is a risk of unreliable results for some CLs.

Author details


Oleh Velychko^{1*} and Tetyana Gordiyenko²

1 State Enterprise “Ukrmetrteststandard”, Kyiv, Ukraine

2 State University of Telecommunications, Kyiv, Ukraine

*Address all correspondence to: velychko@ukrcsm.kiev.ua

IntechOpen

© 2021 The Author(s). Licensee IntechOpen. This chapter is distributed under the terms of the Creative Commons Attribution License (<http://creativecommons.org/licenses/by/3.0>), which permits unrestricted use, distribution, and reproduction in any medium, provided the original work is properly cited. 

References

- [1] ILAC B7:10/2015. The ILAC Mutual Recognition Arrangement, ILAC, 2015; 8 p.
- [2] ILAC P4:05/2019. ILAC Mutual Recognition Arrangement: Policy and Management, ILAC, 2019, 11 p.
- [3] ILAC P5:05/2019 ILAC Mutual Recognition Arrangement: Scope and Obligations, ILAC; 2019, 9 p.
- [4] Velychko O., Gordiyenko T. Metrological Traceability at Different Measurement Levels. Standards, Methods and Solutions of Metrology, Published by IntechOpen, London, United Kingdom, 2019; Chapter 1, pp. 1–21. DOI: 10.5772/intechopen.84853.
- [5] ILAC P9:06/2014 ILAC Policy for Participation in Proficiency Testing Activities, ILAC; 2014, 8 p.
- [6] ILAC P10:07/2020. ILAC Policy on Traceability of Measurement Results, ILAC; 2020, 11 p.
- [7] ILAC P14:09/2020 ILAC Policy for Measurement Uncertainty in Calibration, ILAC; 2020, 14 p.
- [8] JCGM 100:2008. Evaluation of measurement data – Guide to the expression of uncertainty in measurement (GUM), JCGM; 2008. 134 p.
- [9] JCGM 100:2008. Evaluation of measurement data — Supplement 1 to the “Guide to the expression of uncertainty in measurement” – Propagation of distributions using a Monte Carlo method, JCGM; 2008. 90 p.
- [10] JCGM 104:2009. Evaluation of measurement data – An introduction to the “Guide to the expression of uncertainty in measurement” and related documents, JCGM; 2009. 28 p.
- [11] JCGM GUM-6:2020. Guide to the expression of uncertainty in measurement – Part 6: Developing and using measurement models, JCGM; 2020. 103 p.
- [12] ILAC–BIPM Partnership [Internet]. Available from: <https://ilac.org/about-ilac/partnerships/international-partners/bipm/> [Accessed: 2021-06-25].
- [13] ILAC G17:01/2021. ILAC Guidelines for Measurement Uncertainty in Testing, ILAC; 2021, 12 p.
- [14] ISO/IEC 17025:2017. General requirements for the competence of testing and calibration laboratories. Switzerland: ISO/IEC; 2017. 30 p.
- [15] ISO/IEC 17043:2010. Conformity assessment. General requirements for proficiency testing. Switzerland: ISO/IEC; 2010. 39 p.
- [16] Beckert S. F., Fischer G. E. Interlaboratory comparison of roughness measurement: Application of Algorithm A of ISO 13528:2015 in determining the designated value and the standard deviation. XXII World Congress of the International Measurement Confederation (IMEKO 2018). Journal of Physics: Conf. Series. IOP Publication. 2018;1065;082007:4. DOI: 10.1088/1742-6596/1065/8/082007.
- [17] Iacobescu F., Poenaru M. M., Anghel M.-A. Reactive Power Quality Assessment through Interlaboratories Comparison. 22th IMEKO TC 4 Symposium “Supporting World development through electrical and electronic measurements”, 2017; Iasi, Romania, 13–19.
- [18] Poenaru M. M., Iacobescu F., Anghel M.-A. Length calibration Quality assessment through Interlaboratories Comparison. 22th IMEKO TC 4

Symposium “Supporting World development through electrical and electronic measurements”, 2017; Iasi, Romania, 20–26.

[19] Poenaru M. M., Iacobescu F., Anghel M.-A. Pressure Calibration Quality Assessment through Interlaboratories Comparison. 22th IMEKO TC 4 Symposium “Supporting World development through electrical and electronic measurements”, 2017; Iasi, Romania, 27–32.

[20] Poenaru M. M., Iacobescu F., Anghel A.-C., Salceanu A., Anghel M.-A. Active power quality assessment through interlaboratories comparison, 21st IMEKO TC4 International Symposium and 19th International Workshop on ADC Modelling and Testing Understanding the World through Electrical and Electronic Measurement, Budapest, Hungary, 2016, 224–228.

[21] Furuichi N., Terao Y., Ogawa S., Cordova L., Shimada T. Inter-laboratory comparison of small water flow calibration facilities with extremely low uncertainty. *Measurement*, 2016;91: 548–556.

[22] Bermanec L. G., Zvizdic D. Interlaboratory comparison in the pressure range from 0 to 2 MPa for accredited calibration laboratories. *Int. J. Metrol. Qual. Eng.*, 2015;6, 307. DOI: 10.1051/ijmqe/2015021.

[23] Claudio J., Costa M. Brazilian energy interlaboratory program applicative. In: *Proceedings of the XX IMEKO World Congress “Metrology for Green Growth”*; 2012; Busan, Republic of Korea. IMEKO; 2012. 6 p.

[24] Briggs P. Proficiency testing for calibration laboratories. In: *Proceedings of the XX IMEKO World Congress “Metrology for Green Growth”*; 2012; Busan, Republic of Korea. IMEKO; 2012. 5 p.

[25] Velychko O., Gordiyenko T. The estimation of the measurement results with using statistical methods. *Journal of Physics: Conf. Series*. 2015; 588; 012017:6. DOI: 10.1088/1742-6596/588/1/012017.

[26] ISO 13528:2015. Statistical methods for use in proficiency testing by interlaboratory comparisons. Switzerland: ISO; 2015. 89 p.

[27] Velychko O., Gordiyenko T. The implementation of general guides and standards on regional level in the field of metrology. *Journal of Physics: Conf. Series*. 2010; 238;012044:6. DOI: 10.1088/1742-6596/238/1/012044.

[28] Chunovkina A., Zviagin N., Burmistrova N. Interlaboratory comparisons. Practical approach for data evaluation. In: *Proceedings of the XX IMEKO World Congress “Metrology for Green Growth”*; 2012; Busan, Republic of Korea. IMEKO; 2012. 5 p.

[29] Jackson G. S., Muzikar P., Goehring B. A Bayesian approach to an interlaboratory comparison. *Chemometrics and Intelligent Laboratory Systems*, (2015) Vol. 141, 94–99

[30] Acko B., Brezovnik S., Sluban B. Verification of Software Applications for Evaluating Interlaboratory Comparison Results. *Procedia Engineering*. 2014;69, 263–272.

[31] EA-04/02 M. Evaluation of the Uncertainty of Measurement in Calibration. EA; 2013. 75 p.

[32] Velychko O., Gordiyenko T., Boriak K. Linking the Results of Inter-laboratory Comparisons for DC Electrical Resistance Measures. *Ukrainian Metrological Journal*. 2020;1: 4–11. DOI: 10.24027/2306-7039.1.2020. 204155.

[33] Velychko O., Shevkun S., Mescheriak O., Gordiyenko T.,

- Kursini S. Interlaboratory comparisons of the calibration results of signal generator. *Eastern-European Journal of Enterprise Technologies*. 2019;3/9(99): 14–20. DOI: 10.15587/1729-4061.2019.166504.
- [34] Velychko O., Shevkun S., Gordiyenko T., Mescheriak O. Interlaboratory comparisons of the calibration results of time meters. *Eastern-European Journal of Enterprise Technologies*. 2018;1/9(91): 4–11. DOI: 10.15587/1729-4061.2018.121089.
- [35] Velychko O., Isaiev V. Interlaboratory comparison in context of inappropriate results of voltage thermal converter calibration. *Journal of Electrical Engineering and Information Technologies*. 2018;3;1–2:5–12.
- [36] The BIPM key comparison database (KCDB) [Internet]. Available from: <http://kcdb.bipm.org/> [Accessed: 2021-06-25].
- [37] Velychko O., Isaiev V. A comparative analysis of AC/DC transfer standards for comparison of national standards. *Eastern-European Journal of Enterprise Technologies. Applied physics*. 2018;6/5(96):14–24. DOI: 10.15587/1729-4061.2018.150459.
- [38] Velychko O., Gordiyenko T. Features of the processing of results and estimation of measurement uncertainty of inter-laboratory comparison for calibration laboratories. *Information Processing Systems*. 2018;4(155):77–83. DOI: 10.30748/soi.2018.155.10.
- [39] Sousa J. J. L., Leitão L. T. S., Costa M. M., Faria M. C. Considerations on the influence of travelling standards instability in an interlaboratory comparison program. In: *Proceedings of the XX IMEKO World Congress “Metrology for Green Growth”*; 2012; Busan, Republic of Korea. IMEKO; 2012. 4 p.
- [40] Berni R., Carobbi C. Alternative statistical analysis of interlaboratory comparison measurement results. In: *Proceedings of the XXI IMEKO World Congress “Measurement in Research and Industry”*; 2015; Prague, Czech Republic. IMEKO; 2015. 5 p.
- [41] Cox M. G. The evaluation of key comparison data: determining the largest consistent subset. *Metrologia*. 2007;44:187–200.
- [42] Cox M. G. The evaluation of key comparison data. *Metrologia*. 2002;39: 589–595. DOI: 10.1088/0026-1394/39/6/10.
- [43] COOMET R/GM/14:2016. Guidelines for data evaluation of COOMET key comparison, COOMET; 2016, 6 p.
- [44] COOMET R/GM/19:2016. Guideline on COOMET supplementary comparison evaluation, COOMET; 2016, 5 p.

We are IntechOpen, the world's leading publisher of Open Access books Built by scientists, for scientists

6,300

Open access books available

171,000

International authors and editors

190M

Downloads

Our authors are among the

154

Countries delivered to

TOP 1%

most cited scientists

12.2%

Contributors from top 500 universities



WEB OF SCIENCE™

Selection of our books indexed in the Book Citation Index
in Web of Science™ Core Collection (BKCI)

Interested in publishing with us?
Contact book.department@intechopen.com

Numbers displayed above are based on latest data collected.
For more information visit www.intechopen.com



New Trends of Optical Measurements

*Oleg Angelsky, Peter Maksymyak, Claudia Zenkova,
Olexander Ushenko and Jun Zheng*

Abstract

Some of the achievements of modern optical metrology are offered for the reader at this chapter. Optical testing methods have always attracted by their important advantages: distance, non-destructive impact on the test object and, of course, high accuracy. So, using of polarization optics approach, the authors were able to implement the methods for controlling the surface roughness for the moving surface with the measurement accuracy of 10 angstroms. It has become possible to make a breakthrough in the basic methods of measurements from the nano to the femto or pico units of the measured quantity value over the past decades. Control of nano (micro) particle motion by an optical field and their use for testing complex optical fields; ultra-precise determination of the optical parameters of both solid and liquid and gas-like substances by optical methods; by interference methods and many other, are proposed for consideration here. Some biomedical applications are also offered for reader's familiarization. Particularly, the results of 3D Stokes-polarimetric mapping of microscopic biological images with digital holographic reproduction of layer-by-layer ellipticity polarization maps in differential diagnosis of benign and malignant tumors with different degrees of differentiation are presented. The authors have shown that using of polarization-holographic measurements in biomedical applications makes it possible to obtain a reliable diagnostic of pathological states both of biological fluids and solid-state objects.

Keywords: micro- (nano)- object, optical force, spin (orbital) momentum, biological image, interference method, measurement accuracy, measured value, error

1. Introduction

Metrology is a field of scientific and technical research that has absorbed optical engineering and precision measurements, directions that intensively develop.

This is proclaimed by the world achievements in the creation of femtosecond lasers (John L. Hall and Theodor W. Hänsch “for their contributions to the development of laser-based precision spectroscopy, including the optical frequency comb technique”, Nobel Prize in Physics 2005), the making and successful operation of an optical fluorescence microscope with a record resolution of 10 nanometers (Eric Betzig, Stefan W. Hell and William E. Moerner “for the development of super-resolved fluorescence microscopy”, Nobel Prize in Chemistry 2014) [1], and the intensive research in the development and use of optical tweezers, manipulators,

molecular motors, etc. (Arthur Ashkin “for the optical tweezers and their application to biological systems”, Nobel Prize in Physics 2018).

Using the opportunity of optical diagnostics, observation, and measurement, which are opening up thanks to the development of modern methods for the formation of various features of structured light [2], it has become possible to reach the verge of a picometer level resolution of measurements in a practically revolutionary way.

Already today, ways of implementing the measurement of optical field parameters in three-dimensional space [3–5] with nanometer resolution have been outlined. The appropriateness and importance of such measurements are strengthened in the case of study of polarized light transformations and the possibility of realization an ultra-high resolution in the optical range. In this sense, it is necessary to present some biomedical application and to notice the development and experimental testing of a new 3D Stokes-polarimetry method based on mapping of object fields of biological optically anisotropic layers [6, 7]. Here digital holographic layer – by – layer reconstruction of polarization ellipticity distributions is used, e.g. for express diagnosis and differentiation of samples of polycrystalline blood films of patients with prostate tumors [8–10].

The today’s state of physics and life sciences, in general, require expanding the abilities of optical systems by moving from the systems of the so-called millimeter-micrometer range to instruments and devices operating in the nano-, pico-, femto-meter ranges.

The implementation of such tasks is impossible without finding and discovering new technical and technological solutions, the creation of hybrid measurement systems that can simultaneously work in different spectral ranges, using different parameters of the optical radiation field for diagnostics, and evidently their interconnection.

A review of the state of research at this level is based on a platform that has been formed in a number of directions by the authors of this chapter.

So, the goal of this presentation is to analyze new trends of precision measurements in the picometer range, based largely on the results of own research by the authors.

2. Micro and nanostructures and metrology applications

2.1 Using of micro- and nanoparticles for metrology

A new unique tool that has appeared relatively recently and enables optical measurement to be carried out, is a set of methods for capturing, moving, manipulating, controlling of the micro- and nanoparticles motion. To this end, optical traps are created in which optical flows can be controlled using a set of field parameters, namely, amplitude, phase, or polarization.

Thus, various types of traps are formed for spatial capture and movement of nanoscale objects, creating active optical forces of the order of femtonewton [11–13].

Comprehensively considering the methods of creating micro- and nano-manipulators, tweezers and motors, as well as using me elements, according to our work [11–14], based on classical optical principles, but supplemented with new, and possibly fundamentally new technical and technological solutions for auxiliary devices, new technical problems for optical measurements of micro-, nano - pico femtosecond ranges are solved. Even in the fact that by the speed of microparticles rotation one can determine the absorption coefficient of a matter, the degree of anisotropy of the material, etc. Basically, it can be claimed that these solutions are built on differential, comparative principles and approaches.

2.2 Biaxial crystals in the tasks of creating multifunctional traps for micro- and nano-objects

Based on modern measurement approaches to achieve a nano (femto) units of optical measurements, the possibility for formation of various amplitude-phase, polarization field structures that can be used for manipulating micro- and nano-objects is shown in [12–14]. An interesting solution to this problem is that due to the use of birefringent crystals, it is possible to simultaneously work with various parameters of the optical field, creating a wide arsenal of traps based on one crystal.

Created traps, trapping nanoparticle by an optical field provide determination of nanoparticle parameters with an error of several percent [15].

So the use of birefringent crystals sets the formation of optical fields with deep structure of the inner energy flows. Spread of a slightly divergent (conical) light beam with prescribed linear polarization generates a complicated optical field with spatially inhomogeneous distributions of intensity, phase and polarization that is accompanied by an intricate pattern of the transverse energy flows (**Figure 1**). Here the reader can estimate field distributions at the biaxial crystal output in the vicinity of the optical axis O. Both axes lie in the plane (XZ) so that $x = 0$ corresponds to the middle direction between the axes. The input beam polarization makes an angle 45° with axis X. **Figure 1a** presents both intensity distribution after the output X-oriented polarizer (background) and the transverse orbital flow of the X-polarized component (black arrows). The spin density of the total output field (background), the spin flow map (cyan arrows) and the polarization distribution (gray ellipses) are described in **Figure 1b**.

Such fields offer a variety of possibilities for microparticles' trapping and control, for example:

- the intensity minima (maxima) form natural traps for absorbing (dielectric) particles due to the gradient force [16, 17];
- phase singularities associated with the amplitude zeros (**Figure 1**) are coupled with the vortex-like orbital flows able to induce rotation of the trapped particle;

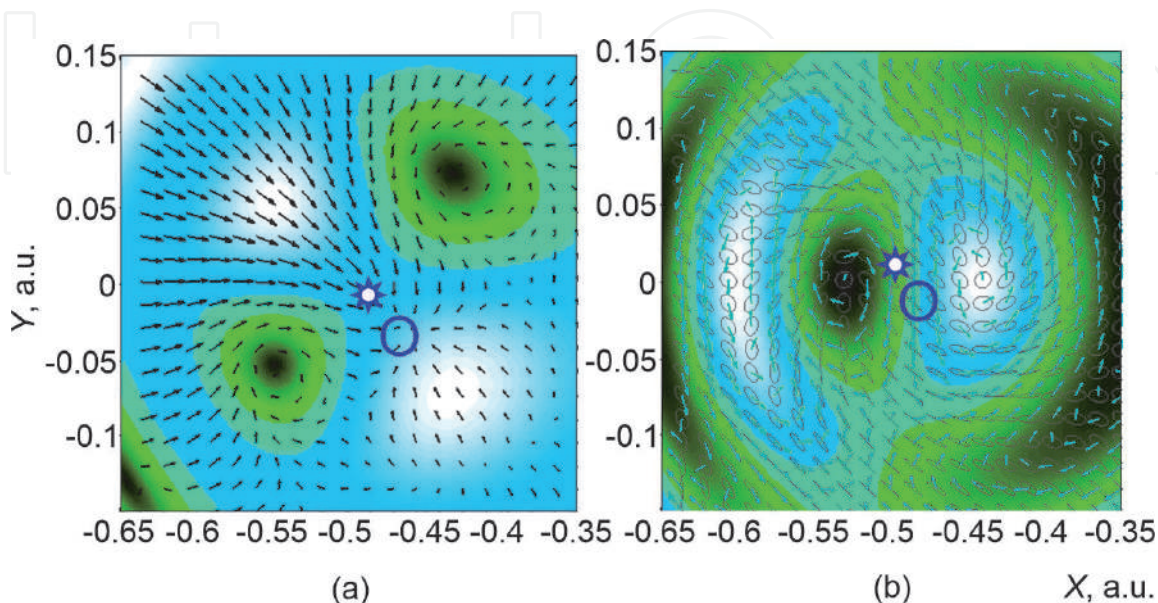


Figure 1.
The scheme of intensity (a), polarization (b) and energy flow (a,b) distribution formed by a birefringent crystal.

- c. both the orbital and spin flows can induce definite motion of particles in the transverse plane (**Figure 1a** and **b**);
- d. the density of spin angular momentum (**Figure 1b**) may induce controllable orbital motion of particles depending on their position within the beam cross section;
- e. the output pattern of optical field distribution can be easily modified via the controllable input and output polarization, providing suitable means for delicate spatial positioning of the trapped particles.

Arrangement of an optical tweezer employing the above principles is shown in **Figure 2**. This optical arrangement based on a birefringent crystal consists from a laser (1) (650 nm, 200 mW), quarter-wave plate – 2, two polarizers – 3, 11, beam expander with spatial filtering – 4, mirror – 5, microobjectives – 6, 8, 13, 17, biaxial crystal with 3D rotating drive – 7, calcite plate – 9, calcite wedges with 2D shifting of one wedge – 10, beam-splitting dichroic cube – 12, sample – 14, white-light source – 15, condenser lenses – 16, CCD-camera – 18, Personal Computer (PC) – 19.

On the other hand, as already noted, the use of nano and micro particles provides a diagnostic tool for optical fields. The optical forces arising in the optical field and acting on these particles are at the nano-, pico- femto- Newton, differing in accordance with the properties, shape and size of the particles. Accordingly, it becomes possible to spatially separate internal optical flows, both with respect to spin and orbitally one.

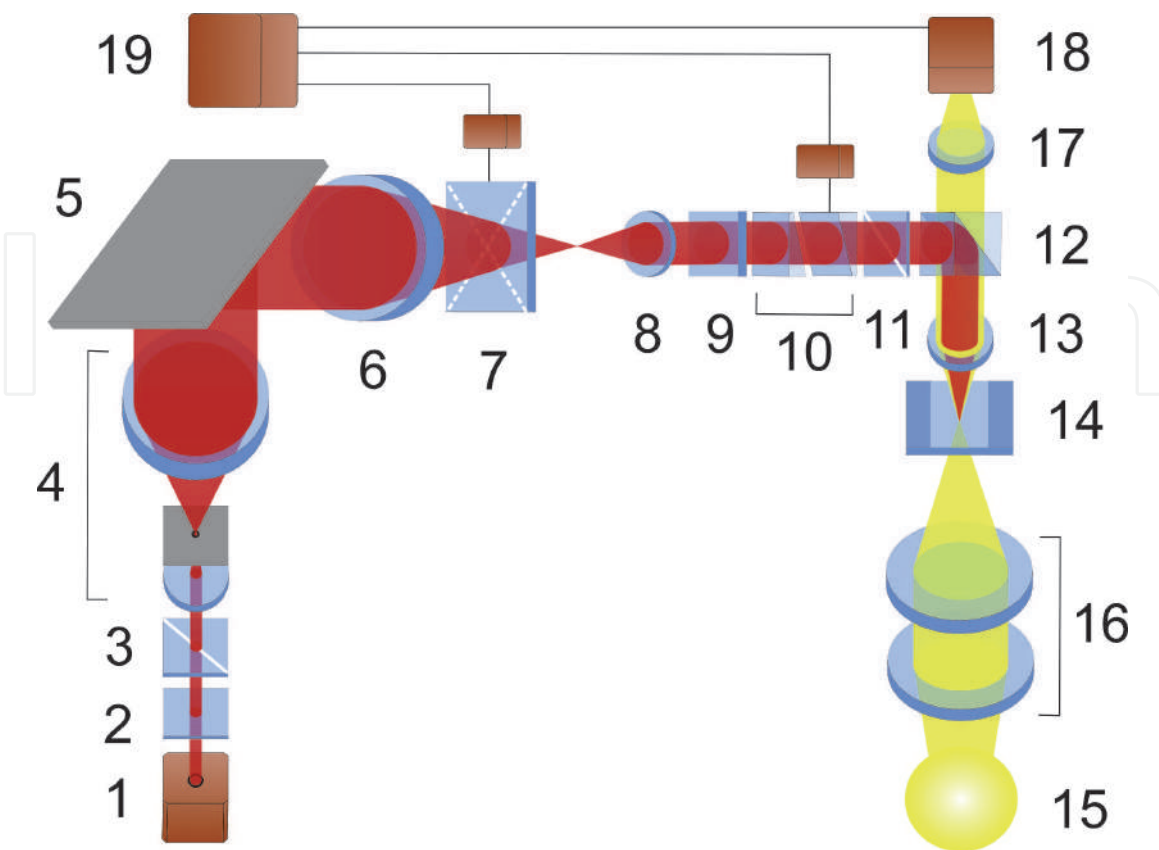


Figure 2.
Optical arrangement of tweezers based on a birefringent crystal.

2.3 Micro and nanoparticles as field probes

Our next achievements [11–14] demonstrate the results obtained by separating the contribution of the orbital and spin angular momentum to the total picture of trapped particles motion in the optical field.

To identify the internal spin energy flows [12], it was necessary to analyze the mechanical action of the spin momentum by testing, selecting size and property of the particles. The spin momentum manifests itself “in its pure form” with all the specific properties in the situation of a symmetric superposition of circularly polarized plane waves and thus the formation of a circularly polarized field having inhomogeneous energy (**Figure 3**) [11, 13]. The mechanical action of the incident field on test particles, when including the scattering components, was carried out through the calculation of the Cartesian components of the force (F_x , F_y , F_z) acting on particles that are placed in the optical field. The longitudinal component of the force (F_z) represents the traditional action of light pressure, which direct the particles forward; the transverse y-component (F_y) corresponds to the gradient force (F_y^{grad}) of an inhomogeneous optical field and traps particles or repels them from areas of high concentration of electromagnetic energy. The most interesting result is the analysis of the component F_{sp}^{\pm} of the optical power along the transverse direction F_x - the only component of the force that is associated with the spin flow. This conclusion is confirmed by the fact that, in accordance with the behavior of the spin flow, the value of the force F_x changes its sign with a change of the helicity σ of the incident beam. In the case of linearly polarized light, this component of the force completely disappears.

Despite the mechanical equivalence of spin and orbital energy flows, that is, their ability to cause translational or orbital motion of the particles under study, the quantitative features of spin-induced and orbital-induced motion, their dependence on the size and properties of the particles are significantly different. That is, the effect of spin and orbital flows can be experimentally distinguished by using test particles with specially selected size and properties. The following figure (**Figure 4**) [13] shows the dependence of the components' value of the optical forces on the particle size for different types of particles. The calculations were performed for two types of spherical particles suspended in water ($\varepsilon = 1.77$, $\mu = 1$, $n = 1.33$): metal (gold hydrosol, relative refractive index $m = 0.32 + 2.65i$ [18]), dielectric (latex in water, $t = 1.12$); wave number $k = 1.33 \cdot 10^5 \text{ cm}^{-1}$ (He-Ne laser).

To eliminate the influence of the incident beam intensity and reduce the number of data presented, the obtained value of the force was normalized by dividing the calculated values by the total momentum of the incident flow over its cross section (P_0). A comparative picture of the mechanical action of the optical forces associated with the spin and orbital internal energy is presented in **Figure 4**. To compare the

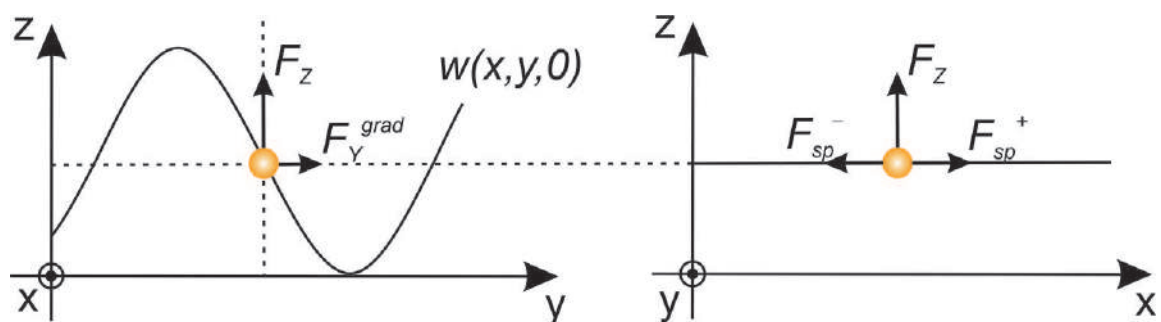


Figure 3.
 The components of optical force distribution.

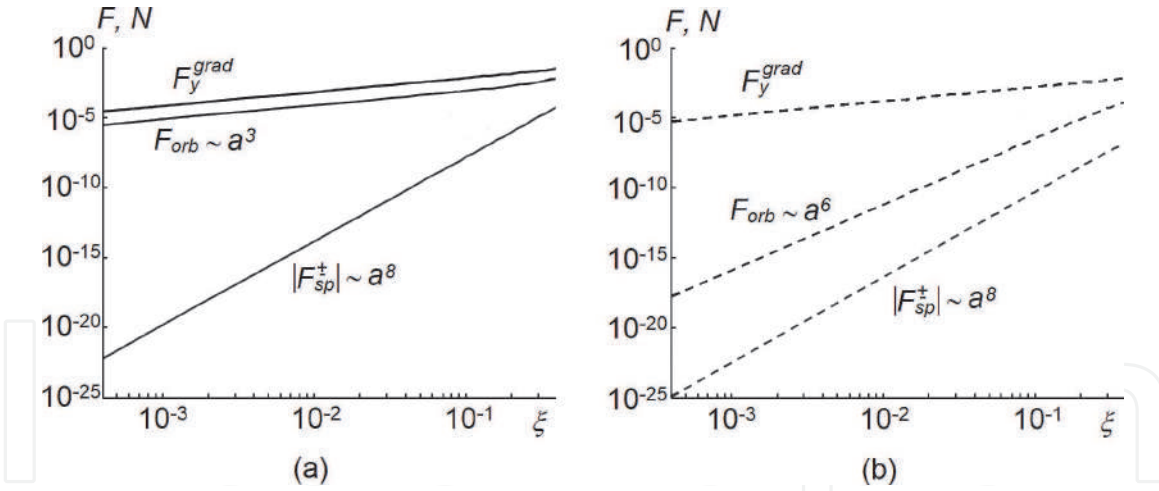


Figure 4.

A comparative picture of the mechanical action of the optical forces associated with the spin and orbital internal energy for different types of particle: a) metal and b) dielectric.

optical force, the gradient force F_y^{grad} is shown. The measured gradient force range is 10^{-4} to 10^{-6} Newton, depends on the particle size and its type and determines the measurement accuracy as 10^{-7} Newton.

The curves are made for particles of small size. Solid lines describe metal particles, dotted lines describe dielectric particles. Here $\xi = ka$ is a dimensionless particle size parameter (a – is the particle radius).

As can be seen from the results of estimating the values of spin and orbital flows shown in the figure, the quantitative features of spin-induced and orbital-induced motions and, accordingly, the generated optical forces, their relationship with the size and properties of the particles are significantly different. Following the main aim of this paper, conducting optical power measurement according to the evaluation results (**Figure 4**), we can note the measured quantity of optical force up to 10^{-15} – 10^{-25} degree for the spin-induced component of the optical force in accordance with the particle size. We managed to carry out experimental confirmation of the existence of a force of this units of Newton in a specially organized experiment [11–13]. The use of dielectric test particles of the Rayleigh light scattering mechanism made it possible to evaluate experimentally the action of spin and orbital flows. Particles are sensitive to optical forces caused both by spin and orbital flows.

Thus, the change of the measured component of the optical force leads to the change of the measurement range of: the value of the optical force associated with the spin internal energy as 10^{-25} to 10^{-10} Newton, for different types and size of particle, with the error of 10% and the value of the optical force associated with the orbital internal energy as 10^{-16} to 10^{-6} Newton with the error of 7%.

The value of the force is estimated at the pico-, femto- Newton, and in accordance to our experiments (**Figure 5**) [11] the obtained results can be considered as a proof of the mechanical action of the spin moment (spin energy flow) of the light beam on test particles of the chosen shape and properties. The experimental observation of the polarization-dependent orbital motion of test particles in a transversely inhomogeneous beam with circular polarization, where the rotational action of the orbital momentum density is absent or insignificant, is here demonstrated. Moreover, this demonstration of motion required an ultra-precise experiment, when the peculiarities of measured quantity of optical force of the femto units of Newton is taken into consideration.

In order to observe the action of optical flows on nanoparticles, an optical scheme was chosen in which the lens aperture was selected in order to avoid

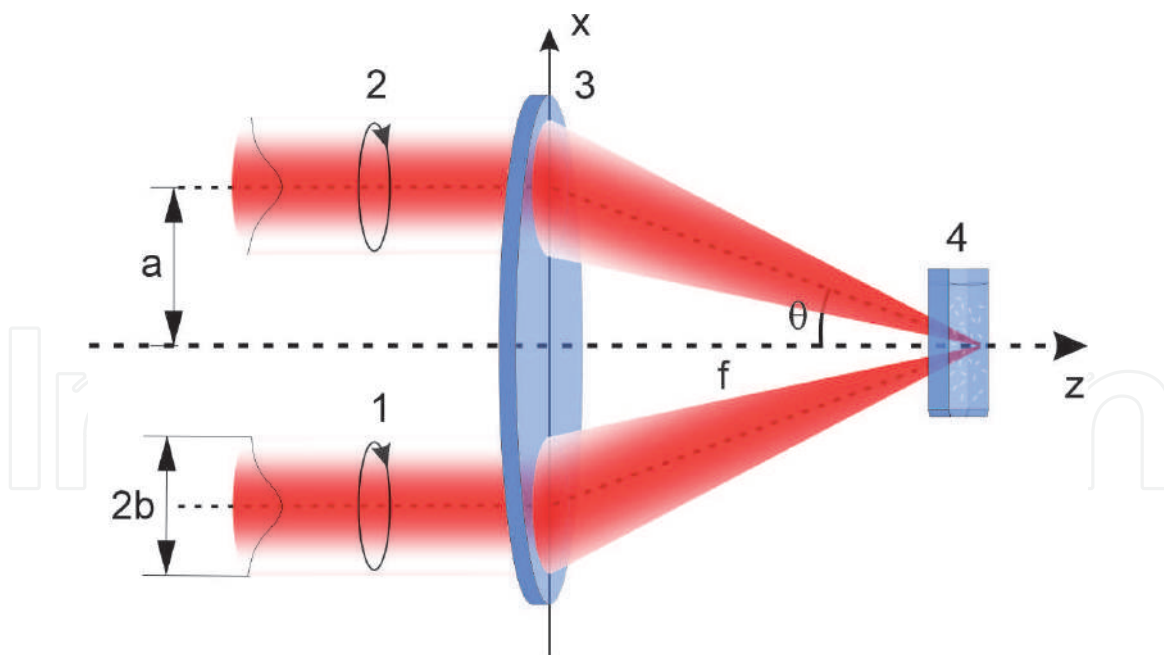


Figure 5.
 Scheme of the experimental setup: (1), (2) - input beams; (3) objective lenses; (4) cuvette with test particles suspended in water.

transforming conversion of spin and orbital flows. Significant numerical apertures do not allow one to study the action of the spin momentum density, since strict focusing of a circularly polarized beam causes a partial transformation of the output spin flow into an orbital one. And even if some mechanical action of the flow is observed, then it is impossible to definitely conclude about the spin or orbital momentum action. To avoid ambiguity, focusing should not be high: the spin-orbital transformation can be neglected (i.e., it does not exceed 1%) when using lenses with a numerical aperture < 0.2 (angle $\theta \approx 11^\circ$).

Such focusing leads to a certain loss of energy concentration; however, a substantial decrease of the spin action in the focal region can be avoided if the decrease in intensity is compensated by an increase of the beam inhomogeneity. The above experimental design made it possible to reproduce and record the action of the optical force at the femto units of Newton, which is a unique confirmation of the present measurements' opportunity. The circulation of energy of a spin nature exists within each band, while the orbital momentum is completely radial and is associated with the beam divergence (**Figure 6**) [11]. This radial field momentum can be used to explain the mechanism of particle capture into the desired position outside the center, which allows one to observe the orbital motion associated with the density of the spin momentum.

In an inhomogeneous light field, any dielectric particle is exposed to the action of the gradient force that directs it to the maximum intensity, for example, to the axis of the beam, and vice versa. The radial density of the orbital momentum of the diverging beam creates a value of radial pressure that directs the particle away from the axis. As a result, both forces cancel each other out in certain areas of the interference pattern.

So, by changing the circulation of the electric field vector, the captured particle carries out orbital motion being it clockwise (**Figure 6A**) or counterclockwise (**Figure 6B**) rotational motion with respect to its own axis. Both the orbital and rotational motions stop when the polarization of the incident beam is linear. The possibility of particle transfer by the force induced by the influence of spin energy flows opens up new prospects for the creation of controlled optical micromachines,

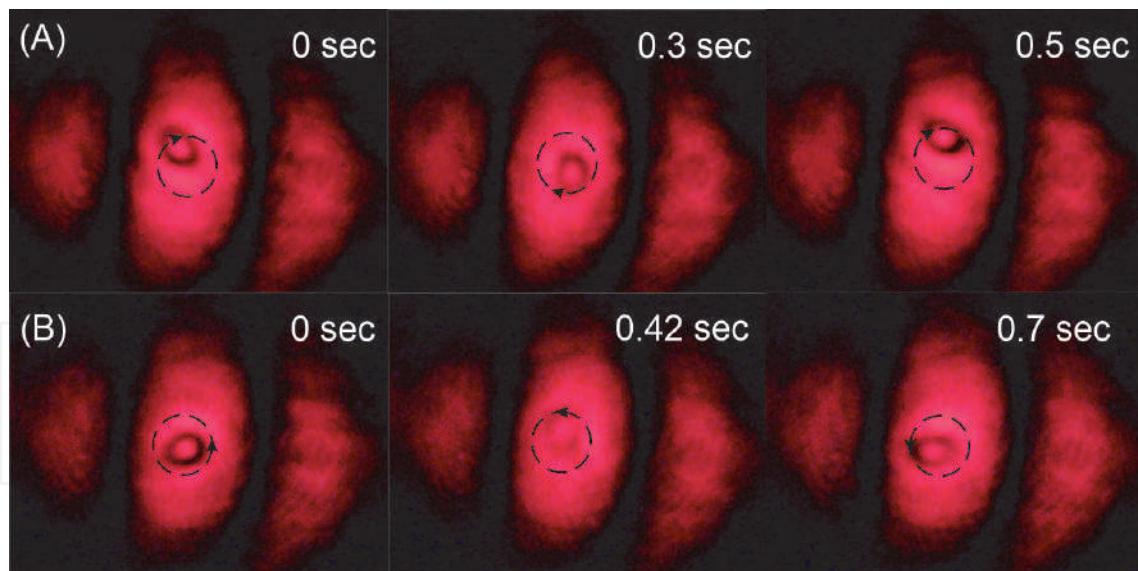


Figure 6.

The position of the captured particles within the center of the interference band at different moment of time with the change of the electric field vector circulation: A) clockwise, B) counterclockwise. The arrows indicate the direction of particle rotation.

micromanipulators in which the regulation and switching are performed through polarization control without changing the beam intensity or its spatial profile. Such methods can be useful in many systems requiring high switching speed.

It should be kept in mind that a nanoparticle is a multifunctional nanoscale tool, playing the role of a separate probe for diagnosing the field structure in the zone of a complex field microdistribution. These nanoparticles are the means of delivering microdoses of drugs into cells, and the unique means of studying complex macro-structure of the optical field in almost real time. Such a possibility can be realized in water or other transparent solutions, when the concentration of nanoparticles in various areas of the complex optical field, their spatial distribution will provide information on the spatial distribution of the amplitude, polarization, and, as a result, the phase of the field. There is an expected forecast for the study of speckle fields by nanoparticles, when they are transferred to the points of field singularity by internal energy flows, making it possible to restore information about changes of macro and micro objects over time.

2.4 Evanescent fields for micro-object manipulation

To talk about the influence of an optical field on nanostructures is necessary in order to distinguish the action of evanescent optical fields of a complex energy distribution, in particular to transfer of microdoses of drugs, providing precise accuracy of the transfer site and the transfer rate of hundreds of nanometers per second [18–20]. This situation becomes possible in the case of excitation of evanescent fields by linearly polarized beams with the azimuth of polarization of 45° . The evanescent field formed in such a way has a special distribution of spin and orbital momentum, it is elliptically polarized, in which the energy circulation is fixed in two planes - a plane parallel to the interface between the two dielectrics, where there is total internal reflection and in the plane perpendicular to it. A specific feature of the excitation of evanescent waves using a linearly polarized wave with azimuth of polarization of 45° is that the transverse spin component, which is responsible for the transverse component of the optical power appears.

In a paper [21], direct measurement of an optical momentum, which is called as extraordinary, and helicity dependent force directed perpendicularly to the

Poynting vector propagation, being proportional to the ellipticity of the local polarization of the probing beam has been reported. Such a complex structure of optical force takes place for evanescent waves and other structured fields being associated with the spin-momentum part of the Poynting vector. The extraordinary transverse momentum has been measured using a femto-newton resolution nano-cantilever immersed in an evanescent optical field above the total internal reflecting glass surface.

In our, later proposed experiments [22, 23], we use a free-standing plate for detection of the influence of an evanescent wave. We demonstrate an optically transparent birefringent microplate motion, influenced by the optical forces generated at the plate plane due to the complex optical force action: caused by the canonical momentum directed along the wavevector and the transversal spin momentum [24] directed perpendicularly to the canonical momentum. In this case it is possible to observe the motion of the plate in the direction, which does not coincide with any of these directions. The surfaces of a birefringent plate are characterized by the negligible roughness. We deposited gold nanoparticles at plate's upper surface to transfer the transverse momentum to the plate.

Elliptically polarized wave formed at a sup-surface layer enables us to estimate the longitudinal and transversal components of the force. Therefore, the vertical spin of an evanescent wave is the source of the last of them.

We simulate the spin and orbital momenta of an evanescent wave when a linearly polarized incidence wave (at second surface - boundary plate-air) with the azimuth of polarization 45° reaches the interface plate-air here undergoing total internal reflection (TIR). In this case, an evanescent wave that propagates in the z-direction, being damped in the x-direction, can be represented by [21, 24].

$$\vec{E}_{ev} = E \exp(-i\omega t) \left(\vec{x} \frac{1}{\sqrt{1+|m|^2}} + \vec{y} \frac{m}{\sqrt{1+|m|^2}} \cdot \frac{k}{k_z} + \vec{z} (-i) \frac{1}{\sqrt{1+|m|^2}} \cdot \frac{k}{k_z} \right) \cdot \exp(ik_z z - \kappa x), \quad (1)$$

where $k_z = k \frac{n_o}{n} \sin \gamma$, $\kappa = k \sqrt{\left(\frac{n_o}{n}\right)^2 \sin^2(\gamma) - 1}$ is the exponential decay rate.

Here, $v m = \frac{T_{\perp}}{T_{\parallel}} m_1$ is a state of polarization of an evanescent wave [24], m_1 is the state of polarization of the beam impinging at the interface plate-air being equal to unity for linear polarization with the azimuth of polarization 45° . γ is the angle of incidence at the surface, where TIR takes place.

$E = \frac{k_z}{k} \sqrt{\frac{\mu_1}{\mu}} T E_0$ is The electrical strength of the field of an evanescent wave,

where $T = \frac{\sqrt{|T_{\parallel}|^2 + |m_1|^2 |T_{\perp}|^2}}{\sqrt{1+|m_1|^2}} \exp[i \arg T_{\parallel}]$ is the transmission coefficient [22], and T_{\parallel}, T_{\perp} are the Fresnel transmission coefficients.

In this case the spin momentum density has both longitudinal and transversal components [24].

Thus, the resulting momentum density in the z-direction possess both orbital and spin momentum density and is given by

$$p_z = p_{oz} + p_{sz} = \frac{A^2}{8\pi\omega} \left[\left(k_z + \frac{m^2 k^2}{k_z} + \frac{\kappa^2}{k_z} \right) - 2 \frac{\kappa^2}{k_z} \right] \exp(-2\kappa x). \quad (2)$$

The transversal momentum caused by the vertical spin is represented as.

$$p_y = p_{sy} = \frac{A^2}{4\pi\omega} \frac{k\kappa}{k_z} \text{Im} m \cdot \exp(-2\kappa x), \text{ where } A = E \frac{1}{\sqrt{1+|m|^2}}.$$

We change the angle of incidence of a beam at the boundary plate-air. It leads to changing of the ellipticity of the evanescent wave above the plate surface. That is why one can suppose that the magnitude of the transversal spin momentum could be characterized by the different dependence towards to the resulting momentum in the longitudinal direction with the main contribution by the canonical momentum. We suppose that momentum is transmitted to the spherical surface S of the gold particles localized at the plate surface. Particle's light-scattering is taken into account within the Mie approximation [24], giving $\vec{F} = \int_S \Delta \vec{p} dS$, where $\Delta \vec{p}$ is the change of momentum density. Simulation of the force affecting a plate and causing its motion presumes integration over the illuminated area with beam aperture of 6° . The results of optical forces simulation in the y - and z -directions for a linearly polarized incident beam with the azimuth of polarization of 45° versus the incidence angle γ are shown in **Figure 7**.

As can be seen from the presented results, the transversal component of the optical force acting from the evanescent field on gold nanoparticles is experimentally fixed in our studies. Experimental study has shown that the motion of the birefringent plate depends on the angle of incidence of the beam which generates the evanescent wave. The incidence angle influence both velocity and spinning of the plate, as well as the angle of deviation of the ahead motion from the z -axis.

Thus, our experiments [22, 23] demonstrate simultaneous plate rotation and forward plate motion. The rotation of the plate stops in the situation when the main optical axis of the plate coincides with the azimuth of polarization of the incident beam. The compensation of birefringence torques leads to vanishing of plate rotation. This is observed precisely for linearly polarized wave impinging onto the second surface of a plate at an angle $\pm 45^\circ$. It is achieved for an angle of incidence of the probing beam about 58° which gives the azimuth of polarization of this beam at the first plate interface (boundary air-plate) equal to 62° . Therefore, rectilinear motion of the plate without its rotation is possible due to the action of the

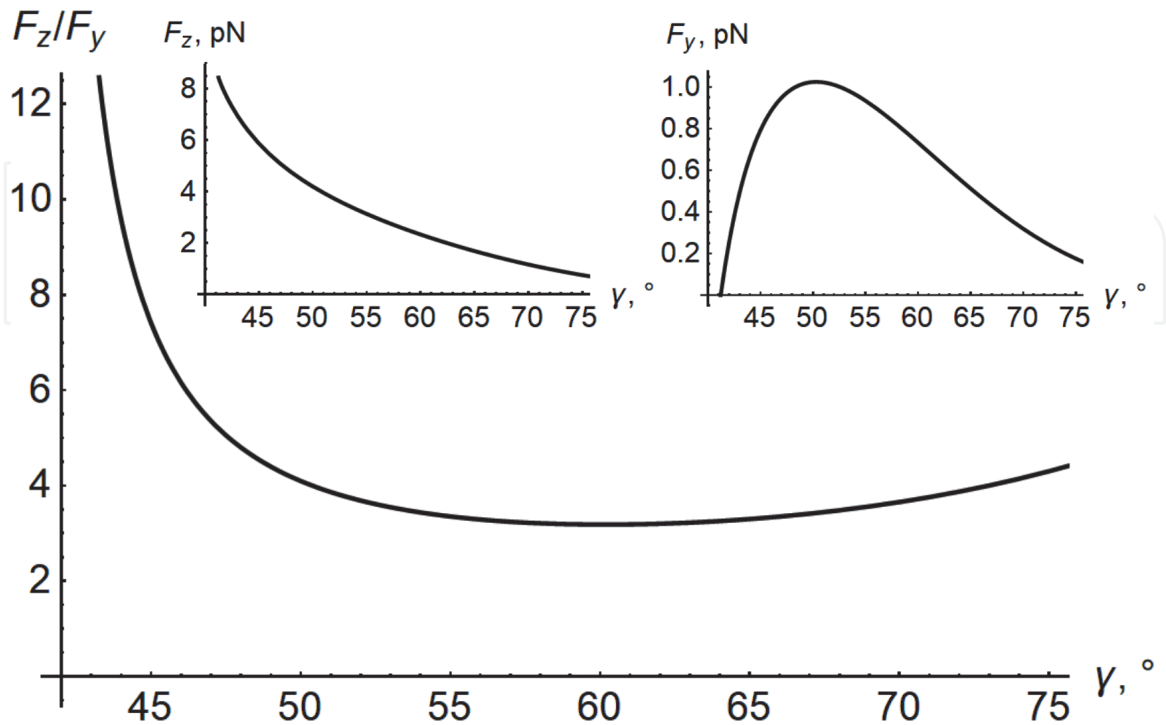


Figure 7. The ratio of optical force in the longitudinal and transversal directions (F_z/F_y) with insets, described the resulting force in the z -direction (F_z) and the transverse diagonal polarization-dependent force induced by the vertical spin momentum in the y -direction (F_y), as a function of the incidence angle γ .

transversal component of the optical force generated above the plate. The angle between the motion direction and z-axis is 15°.

The use of these effects for evanescent waves [25, 26], in particular, is relevant for the development of nanotechnology, including molecular, especially for biomedicine, nano-therapy, transportation of medical products, bio-marking, cancer diagnosis, and bio-probing. All this provides a new tool to investigate the cell properties, i.e. mechanical or optical parameters and characteristics [26].

This brings about non-invasive methods for evaluating and analyzing pathological changes in tissues with the search for new opportunities for treating diseases and possible pathologies by non-traumatic, easily accessible methods.

2.5 Measurement of optical parameters for low-absorbing microparticles

The next step of our paper is to demonstrate one of the solutions for measurement and determining the absorption coefficient of low-absorbing microparticles by estimating the rotation speed of such objects in the field of a circularly polarized beam [27]. The uniqueness of the proposed experimental approach is that the measurement error in determining the optical parameter is of the order of femto units. It is a confirmation of the breakthrough in optical metrology and relies on the fact that modern experimental equipment and corresponding experimental approaches and measurements have gone out of the microrange to a new, more delicate level.

In particular, we present results obtained by studying the microscopic properties of liquids and various biological samples by complex optical fields [28, 29]. The optical field, acting on particles, transfers part of the momentum to them, thereby causing the spatial motion of the particles. The characteristics of this motion substantially depend on the optical constants of the studied micro- and nanoparticles.

Even the properties of complex solid samples containing, as impurities, various kinds of inclusions in the form of a fine-grained structure are determined by the optical properties of these micro and nanoparticles, thereby opening for applications. A change of the radiation propagation conditions substantially depends on the attenuation of the radiation, here determined by the absorption and scattering of radiation on these structures.

Traditionally, solutions to such problems are sought through using of Mie scattering theory, which allows one to determine mechanical ponderomotive factors (force and torque) which an optical field exerts on a particle. More importantly, the ponderomotive factors can be directly associated with the optical parameters of the particle, and this can be employed for their measurement.

In [27], the criterion of optical fields action on micro- and nano-particles is the rotational motion of the particle under the influence of a torque, which is inherent in an optical field of circular polarization with a spin angular momentum. The spinning motion of the particle is due to the field spin angular momentum absorbed by the particle, and its angular velocity Ω is related to the radiation torque by the equation $\Omega = \frac{T}{8\pi\eta r^3}$, where $\eta = 8.9 \cdot 10^{-3} \text{ dyn} \cdot \text{s} \cdot \text{cm}^{-2}$ (at 25°C) is the dynamical viscosity of the medium. T is an absolute torque, which is calculated through Mie theory $T = 4\pi I \frac{n}{\epsilon c} \sigma \left(\text{Im}(\alpha_e) - \frac{2k^3}{3\epsilon} |\alpha_e|^2 \right)$, here α_e – is the polarizability, appears due to the particle absorption. I is the energy flow density in the wave, c is the light velocity in vacuum, ω is the wave frequency, $k = (\omega/c)n$ is its wavenumber, and σ is the wave spin number equal to ± 1 for right (left) circular polarization, respectively, and 0 for any linear or no polarization. Here the particle is assumed to be immersed in a homogeneous isotropic dielectric medium with real permittivity ϵ and real permeability μ so that the refraction index equals to $n = \sqrt{\epsilon\mu}$.

The absorption index κ of the particle suspended in water and trapped in the center of a focused Gaussian beam waist with radius $w_0 = 2 \mu\text{m}$ can be directly derived from the observed spinning velocity Ω exhibited by the particle in the beam with power $P = 100 \text{ mW}$, $\kappa = q \frac{\Omega}{P}$, where q is the transition coefficient. At the same time, the particle must be with low absorption, so that there is no local heating of the medium surrounding the particle. Effective particle capture requires that the particle size be several times smaller than the size of the focusing spot, but in such a way as to prevent diffraction by the captured object. We have used weakly absorbing ($\kappa \leq 10^{-3}$) dielectric particles with diameter 0.5 to $2 \mu\text{m}$. A schematic of the experimental equipment [27] is presented in the following **Figure 8**. This setup consists of a laser – 1, a beam expander with spatial filter – 2, a mirror – 3, a quarter-wave plate – 4, objective lenses – 5, 7 and 8, cell with probing particles suspended in water – 6, CCD-camera – 9, a personal computer – 10, a control unit – 11.

As a result of the optical field action, the particle acquires a rotational motion, and the angular velocity of the particle corresponds to the part of the torque that is absorbed. As absorption increases, acceleration of rotational motion is observed. The measured value of the spinning velocity obtained in the experiment, e.g. for a gamboge particle is of about $\Omega_e = 25.8 \text{ s}^{-1}$, a measurement range of the spinning velocity is $25.8 \text{ s}^{-1} \pm 0.3 \text{ s}^{-1}$, the standard measurement uncertainty is 0.13 s^{-1} with the normal probability distribution. The average measured value of the spinning velocity differs from the theoretically obtained spinning velocity and determines the error of about 20%.

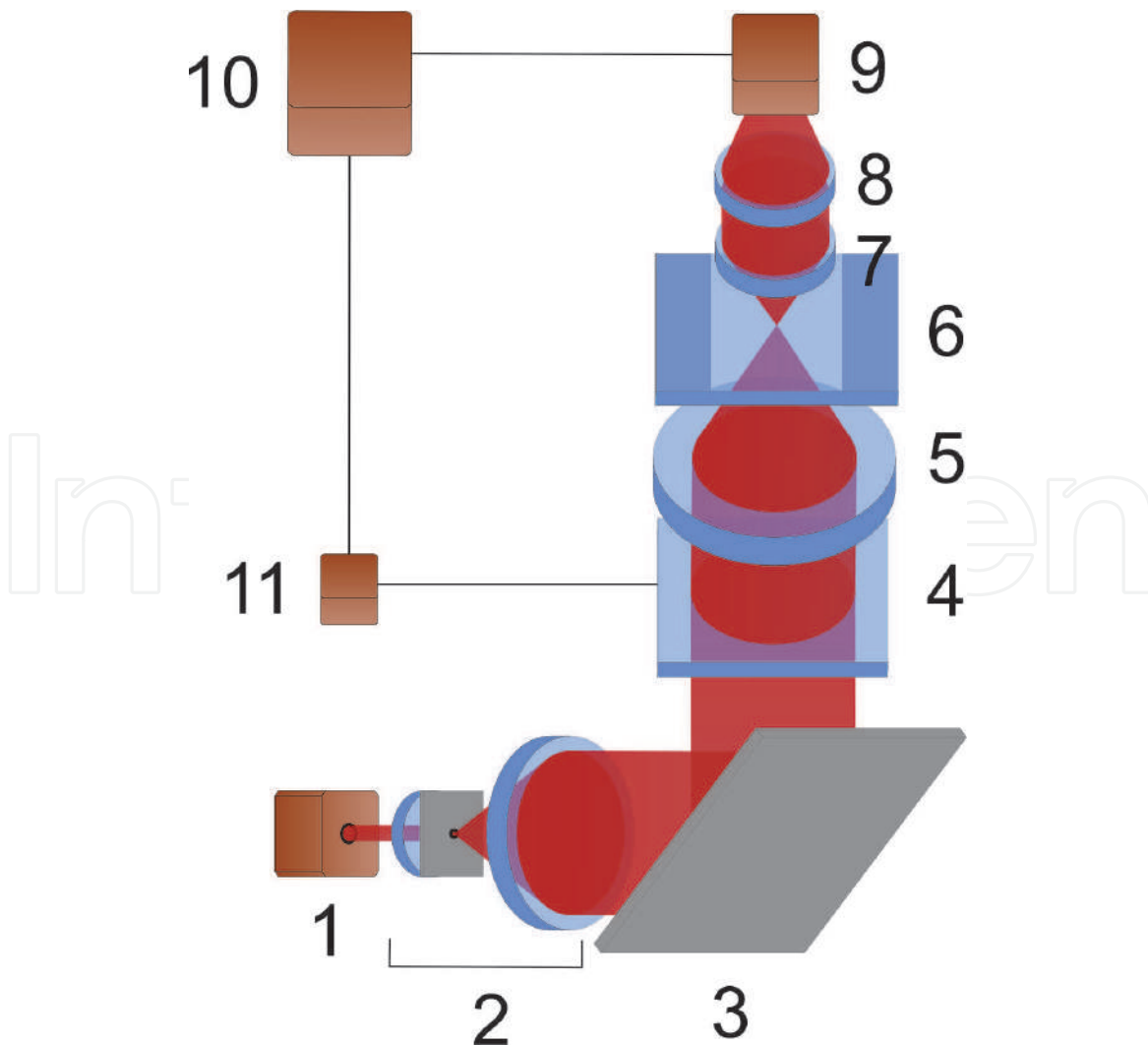


Figure 8.
Schematic of the experimental setup.

Such an error can be explained by the longitudinal displacements of the particle with respect to the beam waist, heating of the cell with particles, changes in the properties of water inside the cell, and other reasons. The introduction of the normalization coefficient, obtained by comparing the theoretical and experimental results, made it possible to determine the value of the particle absorption coefficient, here for this type of particle, it was $12.4 \cdot 10^{-4}$.

Of course, the question arises about the measurement error of the proposed method for measurement the absorption index. The flexibility of this method is determined by the refractive properties of the particle, the density of the medium where the particles are dispersed, the characteristics of the irradiating beam, and the cross-section of the focused beam. Restrictions for the determination of the particle rotation speed of about 0.1 s^{-1} are formed. Then, with the introduction of transition coefficient (q), the error in estimating the absorption coefficient δ can be obtained in the range $10^{-8} \leq \delta \leq 4 \cdot 10^{-7}$. Obtaining reliable results of measurement the absorption coefficient of particles is possible for absorption less than 10^{-2} .

Thus, the possibility of directly assessing the value of the index of light absorption by microparticles became possible thanks to the proposed approach, which uses the principles of capture and rotation of microparticles by internal energy flows. The current state of the development of technology for the manipulation of microobjects of various nature and properties makes the proposed method of measurement of optical properties encouraging and promising for many practical applications. The obtained results are the first step in developing of this kind of measurements. The high sensitivity of the absorption index measurement, the high accuracy of the estimation of the measured parameter, upon reaching the appropriate level of control for the measurement conditions, makes it possible to use this method to study weakly absorbing particles.

The above mentioned results on the involvement of the technique of micro and nanoparticles in the study of complex optical fields, the transition to control of the particle movement within a few angstroms with the acting force on the captured object at the femto Newton unit are opened the new possibilities of modern metrology. Such approaches are already used today to manipulate organelles in cells, to study viscoelastic properties, to build molecular motors and find their implementation among many other interesting applications.

2.6 Surface nanostructure and optical measurements

The next step in presenting the results of research and development on the latest methods of optical metrology is diagnostic methods for processing extremely smooth surfaces with ultra-high precision accuracy [28, 29].

Two techniques for measurement of roughness, based on measurement of a phase variance of the boundary object field and on a transverse coherence function of a field, as well as the devices implementing these techniques were proposed in our papers [28, 29]. The following principles are lying in the base of the proposed techniques:

- heights of surface microirregularities are less than wavelength of the probing radiation, ($R_q < 0.1 \text{ mm}$), and the transversal scale of surface irregularities is larger than a wavelength, so that the specular component of the reflected radiation is present;
- phase variance is measured at the boundary field (the sample surface is imaged at the plane of analysis); the transversal coherence function of a field can be measured at arbitrary zone;

- statistical parameters of a field are measured with interferometric means, within the zero (infinitely extended) interference fringe.
- The first technique (**Figure 9**) is used for measurement of surface roughness based on measurement of a phase variance of the boundary object field [30].

Here the experimental arrangement (**Figure 9**) consists from He-Ne - laser, T - telescope, BS1, BS2- beam-splitters, O1,O2 - objective lenses, S - sample, M - mirror, PM – piezo-ceramic modulator, PD - 2x2 position-sensitive photodetector array, VC- visualization channel, EM - electric motors, AU - automatic zero fringe adjustment unit, COM - comparator, CU - analogue R_q calculation unit, DI - digital indicator.

Using an interrelation among the height parameters of surface roughness and the phase parameters of the boundary object field, one obtains the following

equation for an root mean square deviation (RMS) roughness: $RMS = \frac{\lambda}{4\pi} \sqrt{\frac{\langle I(x,y) \rangle}{I_0}}$.

Technical parameters of the device are the measured RMS range – 0.002 to 0.08 μm , the measurement accuracy - 0.001 μm , the measurement scheme – micro-interferometer, indication rate - one measurement per five second, indicated units – micrometers. Here $I(x,y)$, I_0 are the resulting field and the object beam intensity correspondingly.

This device could be used for measurement of the plane and spherical surfaces with the radius of curvature larger than 0.2 m in polishing machine tool for surface quality control during making of details. This device can be made as a stationary instrument.

The second one is a technique for measurement of surface roughness based on measurement of a field's transverse coherence function (**Figure 10**) [29].

For measurement of the degree of arbitrary surface roughness in the second technique we have proposed an experimental arrangement (**Figure 10**) with

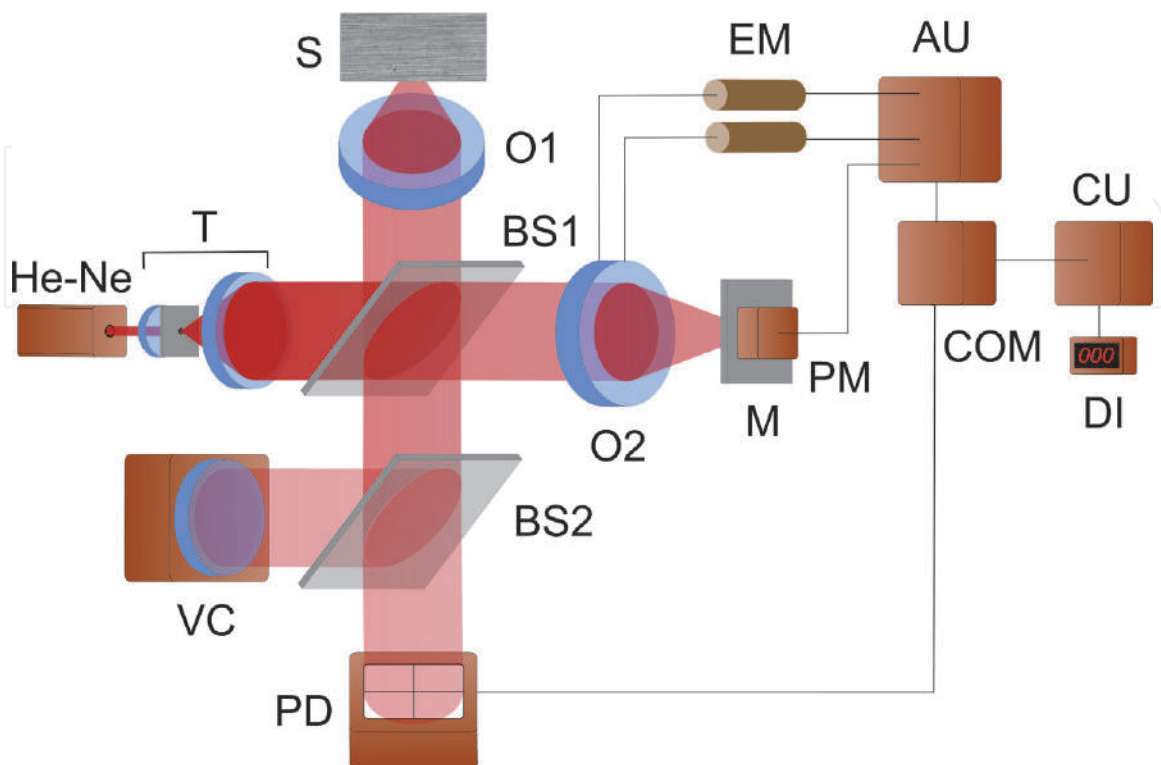


Figure 9.
Experimental arrangement for measurement of the degree of low-reflectance surface roughness.

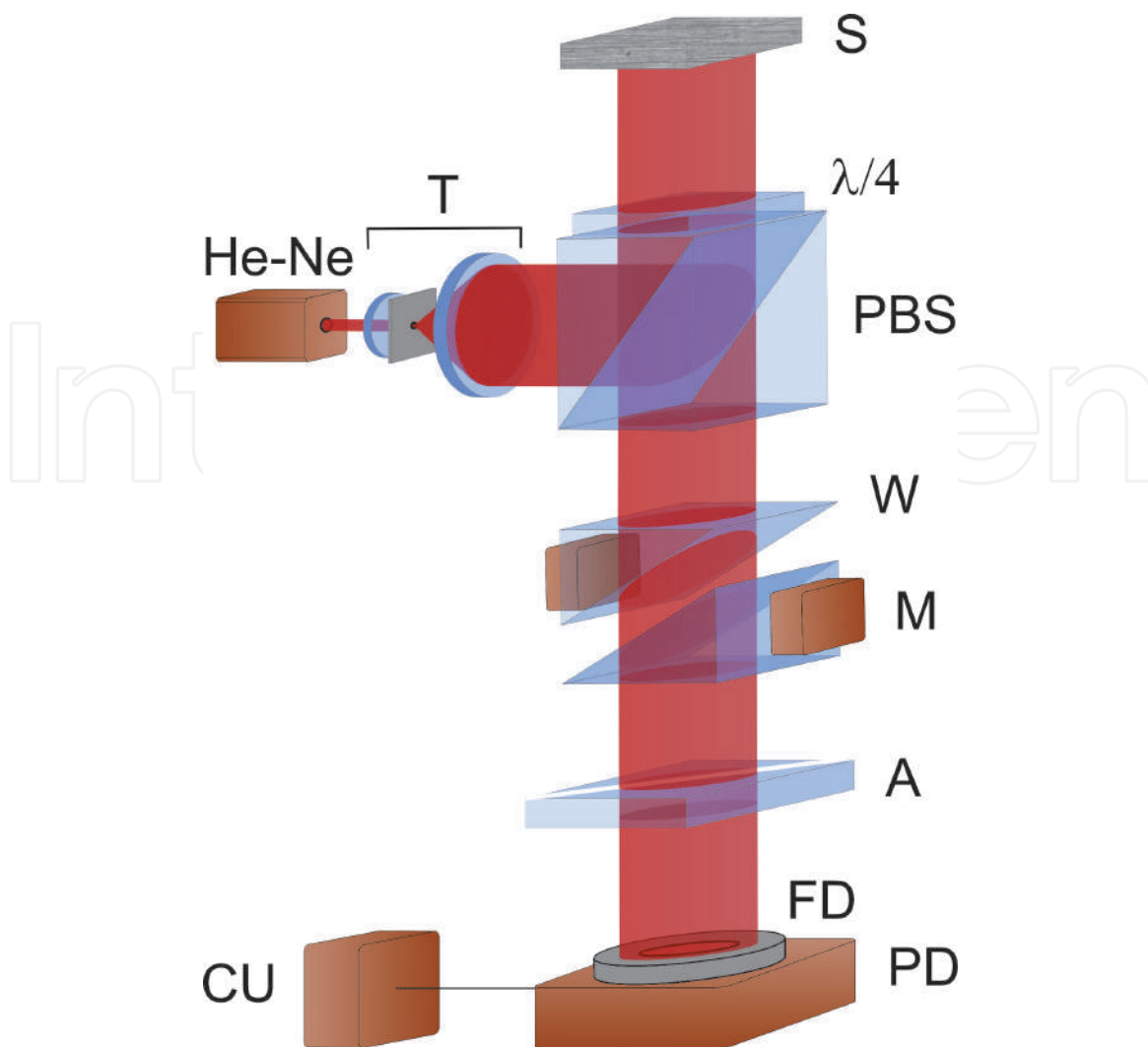


Figure 10.
 Experimental arrangement for measurement of the degree of arbitrary surface roughness.

He-Ne - laser, T - telescope, PBS- polarizing beamsplitter, S - sample, W- calcite wedges; M - electromechanical modulator, A - analyzer; FD - field-of-view diaphragm; PD - photodetector, CU - analogue R_q calculation unit.

Another method for measurement of the phase variance utilizes the relationship between the transverse coherence function $\Gamma_{\perp}(\rho)$ of the scattered field, on the one hand, and the statistical parameters of the object, on the other hand. The RMS height deviation can be found from the relation $RMS = \frac{\lambda}{4\pi} \sqrt{-\ln \frac{I_{max}-I_{min}}{I_{max}+I_{min}}}$, I_{max} , I_{min} are the maximum and minimum resulting intensity, respectively. The information contained in the resulting interference pattern is extracted by transforming the optical signal into electric ones with subsequent processing in the analogue electronic unit CU.

Two versions of the device for a surface roughness control based on measurement of the field's transverse coherence function were displayed:

- A stationary device that can be mounted on the processing tool. Device intended for measurement of the RMS height deviations of slightly rough surfaces over the range from 0.002 μm to 0.06 μm . Technical parameters are measured RMS range – 0.003 to 0.10 μm , measurement accuracy - 0.002 μm . Update rate - one measurement per second. Fields of application are the following: the photochemical industry to analyze the quality of calendar shafts; arbitrarily shaped surfaces with the radius of curvature larger than 0.3 m;

polishing machine tool; space industry to monitor the quality of mirrors fabricated by diamond micro-sharpening. This device was used for surface quality on-line control.

- Portable device for control of large-area or small-area surfaces. Portable device intended for measurement of the RMS height deviations of slightly rough surfaces. Main technical parameters of the device are the measured RMS range – 0.005 to 0.10 μm , the measurement accuracy - 0.002 μm , the update rate - one measurement per second. This device provides the following field of application: device can be made either as a measuring head, or as a stationary instrument, depending on the size and the position of the object to be controlled; polishing machine tool, this device was used for the surface quality control during making of the detail;

Sensitivity of the RMS height parameter of all these devices down to 10 Å was achieved. Roughness control of slightly rough (polished) surfaces with RMS deviation of a profile from a mean surface line ranging from 0.002 μm to 0.10 μm . The technique is applicable to metallic, insulator, semiconductor, and optical surfaces.

2.7 Optical refractive index measurement

At last it would like to bring one more aspect of fine measurement related to the determination of such an optical parameter of the studied object as the refractive index of light-scattering liquid media. Here, a specific issue is polarization interferometry to find the refractive index of solutions, suspensions and gaseous media [31]. According to the proposed approach [31], a two-beam interferometer is used to determine the refractive index, in which a circularly polarized beam is formed in each channel. The measurement method consists in splitting the optical radiation into two components and forming mutually orthogonal circular polarizations of the field components. As a result of superposition of such beams, a uniform intensity distribution is seen in the interference plane. In this case, the formed field has some deterministic polarization. The resulting field is linearly polarized and is characterized by the azimuth of polarization α_0 . When the studied solution is located in the object channel giving rise to polarization change of the transmitted radiation.

As a result, a rotation of the azimuth of linear polarization is observed in the interference plane, which takes on the value α . That is, the difference in polarization azimuth $\alpha - \alpha_0$, which is related to the reduced path difference of the beams in the arms of the interferometer, and is given by $n = n_0 + \Delta n_0 = n_0 + \frac{(\alpha - \alpha_0)\lambda}{2\pi l_0}$, where n_0 is the refractive index of the main medium (solvent), l_0 is the cell thickness.

The azimuth of polarization of the resulting distribution is sensitive to variations in the path difference in the arms of the interferometer. Even with a change in the path difference between the orthogonal components by an amount less than λ , the polarization azimuth will change significantly. If the path difference between the orthogonal components is λ , then the polarization azimuth will change by 2π . The polarization azimuth can be measured with a measurement error of some seconds. As a result, the accuracy of path difference measurement (Δl) is $10^{-5}\lambda$, and the measurement accuracy of the value of the refractive index is $10^{-6} \frac{\lambda}{l_0}$.

2.8 Biomedical application of 3D laser polarization metrology

Now we will try to present some last results on the development and experimental testing of a new 3D Stokes-polarimetry method for mapping the object fields

of biological optically anisotropic layers [8–10]. Particular, we propose digital holographic layer-by-layer reconstruction of polarization ellipticity distributions to express diagnostic and differentiate of polycrystalline blood films samples of patients with prostate tumors. The structural-logical diagram and design of 3D layer-by-layer Stokes-polarimetry method are described by **Table 1**.

The proposed optical scheme is shown in **Figure 11**.

Collimator 2 forms a parallel ($\varnothing = 2 \times 10^3 \mu\text{m}$) beam of He-Ne ($\lambda = 0.6328 \mu\text{m}$) laser 1, which is divided by 50% beam splitter 3 into “irradiating” (*Ir*) and “reference” (*Re*) ones. The “irradiating” beam is directed through the polarizing filter 6–8 by the rotating mirror 4 on the sample of the biological layer 9. The polarization-inhomogeneous image of the object 9 is projected by the lens 10 into the plane of the digital camera 15. The “reference” beam is forwarded by the mirror

1	Optical probing source	Gas helium-neon laser; Wavelength 0.6328 μm
2	Block for forming the spatial structure of the optical probe	Optical collimator for forming a parallel laser beam with a cross section of 5 mm
3	Block for the formation of the polarization structure of the optical probe	System of formation of linear (0°, 90°, 45°) and right-circular polarization (linear polarizer.
4	Object block	Microscopic coordinate node
5	Formation block of microscopic image	Polarizing micro lens
6	Multichannel polarization filtering block	Transmission system of linearly (0°, 90°, 45°, 135°), right- and left-circularly polarized components
7	Reference wave formation block	Polarizing beam splitter
8	Block for the formation of the polarization structure of the reference coherent wave	Linear (0°, 90°, 45°) and right-circular polarization system
9	Polarization filtering block	Linear polarizer
10	Discritization block	Digital CCD camera
11	Block for computer processing of polarization interferometry data	Calculation algorithms: <ul style="list-style-type: none">• distributions of the magnitude of the ellipticity• statistical moments of the 1st - 4th orders.

Table 1.
Structural-logical diagram of the method of 3D layer-by-layer stokes-polarimetry.

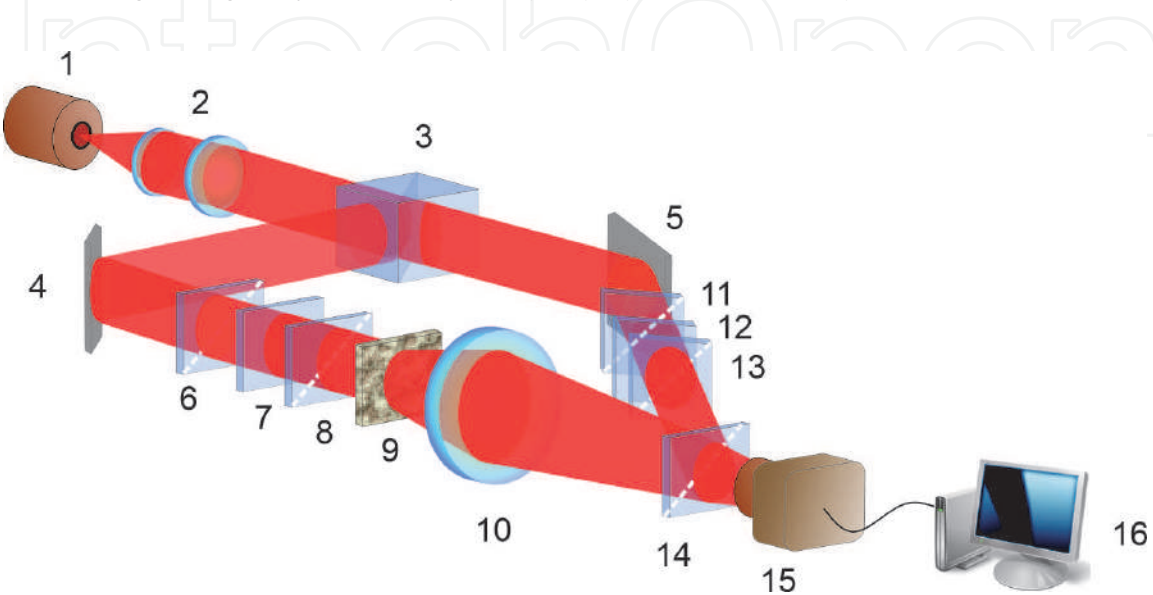


Figure 11.
Optical scheme of 3D Stokes-polarimetry for polycrystalline blood films microscopic images.

5 through polarizing filter 11–13 into the object image plane 9. The resulting interference pattern is recorded by a digital camera 15 through the polarizer 14.

As a result, the topographic maps and histograms of statistical parameters and polarization ellipticity of layer-by-layer digital microscopic images of polycrystalline blood films of patients were measured and compared. It made possible to carry out a differential diagnostic of benign and malignant prostate tumors with different degrees of differentiation.

3. Conclusions

The results presented in this chapter provide an overview of the new approaches of measurements and results obtained by the authors of this chapter over the past decades, in the direction of ultra-sensitive precision measurements. In this chapter we have tried to present the metrological aspects of new optical measurements, that had made it possible to expand the range of measurement of such optical quantities as optical force and optical parameters of solid, liquid and gas up to femto and pico units. This improves the accuracy of optical measurements for the corresponding quantities by 3 orders of magnitude.

The sensitivity of the methods achieved by interference, polarization-interference when assessing the roughness of smooth surfaces, when measurement variations in the refractive index of aqueous solutions ranges from tens of angstroms to tens of nanometers.

The femto unit of optical forces, which occurs in complex optical fields with a rich morphology of the distribution of internal optical energy flows, interacts with micro- and nano-objects of various shapes and properties, but also control their spatial motion in optical traps, the nature of which can differ significantly in accordance with the trap formation mechanism. The optical forces of this physical nature and the values are used to determine the optical parameters of trapped particles, where the error of the determination is controlled at the nanoscale level.

The nature of the trap is different, but the original and new of our approaches are the use of biaxial crystals, which allowed us to form a complex distribution of internal energy flows and at the same time realize the conversion from phase-amplitude to polarization structures intended for nano-objects capture.

New polarimetric solutions for 3D Stokes mapping of microscopic images of polycrystalline blood films with digital holographic reproduction of layer-by-layer polarization maps of ellipticity with the success is shortly demonstrated in the given chapter.

It is clear that this review cannot be a complete analysis of new modern ultrathin methods of optical metrology. It is also worth recalling the ideas and principles of STED microscopy [32, 33], the physical principles of the operation of optical vortex coronagraphs [34], and much more. As an exclusive it could be noted the fundamentally achievable opportunity to operate and manipulate with atoms [2] - this is the ultimate fantasy for the optical range.

IntechOpen

Author details

Oleg Angelsky^{1,2}, Peter Maksymyak², Claudia Zenkova^{1,2}, Olexander Ushenko² and Jun Zheng^{1*}

1 Research Institute of Zhejiang University, Taizhou, China

2 Chernivtsi National University, Chernivtsi, Ukraine

*Address all correspondence to: dbzj@netease.com

IntechOpen

© 2021 The Author(s). Licensee IntechOpen. This chapter is distributed under the terms of the Creative Commons Attribution License (<http://creativecommons.org/licenses/by/3.0>), which permits unrestricted use, distribution, and reproduction in any medium, provided the original work is properly cited. 

References

- [1] Hell S, Nanoscopy with focused light (Nobel Lecture), *Angew. Chem. Int. Ed. Review*. 2015; 54:8054–8066.
- [2] Rubinsztein-Dunlop H. et al., Roadmap on structured light. *J. Opt.* 2017; 19:013001.
- [3] Rotenberg N, Kuipers L, Mapping nanoscale light fields. *Nature Photon.* 2014; 8: 919.
- [4] Bauer T, et al., Observation of optical polarization Möbius strips. *Science*. 2015; 347: 964.
- [5] Geng J, Structured-light 3D surface imaging: a tutorial. *Adv. Opt. Photon.* 2011; 3: 128–133.
- [6] Ghosh N, Tissue polarimetry: concepts, challenges, applications, and outlook. *J. Biomed. Opt.* 2011; 16: 110801.
- [7] Vitkin A, Ghosh N, & de Martino A, Tissue Polarimetry. In: *Photonics: Scientific Foundations, Technology and Applications*. Andrews DL, editors. John Wiley & Sons, Ltd.; 2015, p. 239–321.
- [8] Angelsky OV, Ushenko A, Ushenko YA, Pishak VP & Peresunko AP. Statistical, Correlation, and Topological Approaches in Diagnostics of the Structure and Physiological State of Birefringent Biological Tissues. In *Handbook of Photonics for Biomedical Science*. Tuchin V V. editor. CRC PRESS; 2010, p. 283–322. doi:10.1201/9781439806296-c10
- [9] Ushenko VA, Hogan BT, Dubolazov A, Grechina AV, Boronikhina TV, Gorsky M, Ushenko AG, Ushenko YO, Bykov A, Meglinski I, Embossed topographic depolarisation maps of biological tissues with different morphological structures, *Scientific Reports* 2021; 11(1): 3871.
- [10] Peyvasteh M, Tryfonyuk L, Ushenko V, Syvokorovskay A-V, Dubolazov A, Vanchulyak O, Ushenko A, Ushenko Y, Gorsky M, Sidor M, Tomka Y, Soltys I, Bykov A, Meglinski I, 3D Mueller-matrix-based azimuthal invariant tomography of polycrystalline structure within benign and malignant soft-tissue tumors. *Laser Physics Letters* 2020; 17 (11): 115606.
- [11] Angelsky OV, Bekshaev AYa, Maksimyak PP, Maksimyak AP, Hanson SG, and Zenkova CYu, Orbital rotation without orbital angular momentum: mechanical action of the spin part of the internal energy flow in light beams. *Opt. Express* 2012; 20(4): 3563–3571.
- [12] Angelsky OV, Bekshaev AYa, Maksimyak PP, Maksimyak A., Mokhun II, Hanson SG, Zenkova CYu, and Tyurin AV, Circular motion of particles suspended in a Gaussian beam with circular polarization validates the spin part of the internal energy flow. *Opt. Express* 2012; 20(10): 11351–11356.
- [13] Bekshaev AYa, Angelsky OV, Hanson SG, and Zenkova CYu, Scattering of inhomogeneous circularly polarized optical field and mechanical manifestation of the internal energy flows. *Phys. Rev. A* 2012; 86(2): 023847.
- [14] Zenkova C, Soltys I, Angelsky P, The use of motion peculiarities of particles of the Rayleigh light scattering mechanism for defining the coherence properties of optical fields. *Optica Applicata* 2013; 43(2): 297–312.
- [15] Angelsky OV, Bekshaev AYa, Maksimyak PP, Polyanskii PV, Internal Energy Flows and Optical Trapping. *Optics & Photonics News (OPN)* 2014; 25.
- [16] Dienerowitz M, Mazilu M, Dholakia K, Optical manipulation of

nanoparticles: a review. *J. Nanophoton* 2008; 2: 021875.

[17] Bekshaev AYa, Subwavelength particles in an inhomogeneous light field: Optical forces associated with the spin and orbital energy flows. *J. Opt.* 2013; 15: 044004.

[18] Angelsky OV, Maksymyak PP, Zenkova CYu, Maksymyak AP, Hanson SG, Ivanskyi DI, Peculiarities of control of erythrocytes moving in an evanescent field. *J. of Biomedical Optics* 2019; 24 (5): 055002.

[19] Angelsky OV, Zenkova CYu, Ivanskyi DI, Mechanical action of the transverse spin momentum of an evanescent wave on gold nanoparticles in biological objects media. *Journal of Optoelectronics and Advanced Materials* 2018; 20(5–6): 217–226.

[20] Angelsky OV, Zenkova CY, Maksymyak PP, Maksymyak AP, Ivanskyi DI, Tkachuk VM, Peculiarities of Energy Circulation in Evanescent Field. Application for Red Blood Cells. *Optical Memory and Neural Networks (Information Optics)* 2019; 28(1): 11–20.

[21] Antognozzi M, Bermingham CR, Hoerber H, Dennis MR, Bekshaev AYa, Harniman RL, Simpson S, Senior J, Bliokh KY, Nori F, Direct measurements of the extraordinary optical momentum and transverse spin-dependent force using a nano-cantilever. *Nature Physics* 2016; 12: 731–735.

[22] Angelsky OV, Hanson SG, Maksimyak PP, Maksimyak AP, Zenkova CYu, Polyanskii PV, and Ivanskyi DI, Influence of evanescent wave on birefringent microplates. *Optics Express* 2017; 25(3): 2299.

[23] Zenkova CYu, Ivanskyi DI, Kiyashchuk TV, Optical torques and forces in birefringent microplate. *Optica Applicata* 2017; 47(3): 483–493.

[24] Bliokh KY, Bekshaev AY, Nori F, Extraordinary momentum and spin in evanescent waves, *Nature Communications* 2014; 5.

[25] Yoon Y-Z, and Cicuta P, Optical trapping of colloidal particles and cells by focused evanescent fields using conical lenses. *Opt. Express* 2010; 18(7): 7076.

[26] Gu M, Kuriakose S, Gan X, A single beam near-field laser trap for optical stretching, folding and rotation of erythrocytes. *Opt. Express* 2007; 15(3): 1369.

[27] Angelsky OV, Bekshaev AYa, Maksimyak PP, Maksimyak AP, and Hanson SG, Measurement of small light absorption in microparticles by means of optically induced rotation. *Opt. Express* 2015; 23(6): 7152–7163.

[28] Angelsky OV, Maksimyak PP, Hanson S. *The Use of Optical-Correlation Techniques for Characterizing Scattering Object and Media*. SPIE Press PM71 Bellingham, USA; 1999.

[29] Angelsky OV, Maksimyak PP. Optical correlation diagnostics of surface roughness” in *Optical Correlation Applications and Techniques*. SPIE Press, Bellingham; 2007.

[30] Angelsky OV, Maksimyak PP. Optical correlation diagnostics of surface roughness in coherent-domain optical methods. In: Tuchin VV, editor. *Biomedical Diagnostics Environmental and Material Science*. Kluwer Academic Publishers; 2004.

[31] Angelsky OV, Maksymyak PP, Polyansky VK, Measurement of refractive index of light scattering media (Avtorskoye svidetelstvo). 1986 (in Russian).

[32] Punge A, Rizzoli SO, Jahn R, Wildanger J D, Meyer L, Schonle A,

Kastrup L, Hell SW, 3D reconstruction of high-resolution STED microscope images. *Microscopy Research and Technique* 2008; 71: 644–650.

[33] Vicidomini G, Bianchini P, Diaspro A, STED super-resolved microscopy. *Nat. Methods* 2018; 15: 173–182.

[34] Valle PJ, Fuentes A, Canales VF, Cagigas MA, Villo-Perez I, and Cagigal MP, Digital coronagraph algorithm. *OSA Continuum* 2018; 1(2): 625–633.